

AD-A077 352

HUGHES AIRCRAFT CO CULVER CITY CALIF AEROSPACE GROUP
THERMAL WEAPON SIGHT (TWS). (U)

F/G 17/5

UNCLASSIFIED

SEP 78
HAC-P78-561

DAAK70-77-C-0180
NL

| OF |
ADA
077352



END
DATE
FILMED

1-80

DDC

AD A 077352

LEVEL

2

FORM NO. P78-861
REF. NO. E3829

DDC
RECEIVED
NOV 23 1979
RECEIVED

THERMAL WEAPON SIGHT (TWS)

PHASE I EXTENSION
TECHNICAL SUMMARY REPORT
(CONTRACT DAAK 70-77-C-0180)

SEPTEMBER 1978

AEROSPACE GROUPS

HUGHES

HUGHES AIRCRAFT COMPANY
CULVER CITY, CALIFORNIA

Prepared for

U.S. Army Electronics Command
Night Vision and Electro-Optical Laboratory
Ft. Belvoir, VA 22060

This document has been approved
for public release and sale; its
distribution is unlimited.

79 11 20 134

14 HAC-
P78-561
HAC Ref. E3529

6
THERMAL WEAPON SIGHT (TWS)
Contract No. DAAK 37-77-C-0180

12 55

15

9
PHASE I EXTENSION
TECHNICAL SUMMARY REPORT.

Jan 78 on Phase 1.
June 78

11 Sep 78

Prepared for
U. S. Army Electronics Command
Night Vision and Electro-Optical Laboratory
Ft. Belvoir, VA 22060

AEROSPACE GROUPS
Hughes Aircraft Company • Culver City, California

172 310

slt

CONTENTS

1.0	INTRODUCTION	1-1
I.	Phase I Extension IR Optical Design Activities Summary	1-1
II.	Phase I Extension Mechanical Design Activity Summary	1-10
III.	Phase I Extension MFPA Activities	1-17
APPENDIX A. TWS CAM DESIGN		A-1

Accession For	
NTIS GRA&I	<input checked="" type="checkbox"/>
DDC TAB	<input type="checkbox"/>
Unannounced	<input type="checkbox"/>
Justification	<i>Per the</i>
By	<i>on file</i>
Distribution/	
Availability Codes	
Dist	Avail and/or special
<i>A</i>	

LIST OF ILLUSTRATIONS

Figure		Page
1	Optical Layout of Baseline TWS FLIR Design	1-2
2	TWS FLIR Afocal Telescope Optical Layout	1-3
3	Performance Data	1-4
4	FLIR Imager Optical Layout	1-5
5	COS^4 Losses in Detector Scale	1-6
6	TWS FLIR Afocal Telescopes Performance Data for 8x and 9x Afocal Magnifications	1-7
7	TWS Visual Display (Eye Pupil Excursions at the Exit Pupil)	1-8
8	TWS Visual System Optical Layout	1-9
9	Spherical Cam	1-12
10	Elevation Scan Drive Utilizing a Face Type Cam	1-13
11	Elevation Scan Motion	1-14
12	TWS Scanner Spin-Up Time at Minimum Battery Voltage	1-15
13	TWS Scanner Spin-Up Time at Maximum Battery Voltage	1-15
14	Relative Spectral Response/Watt for Detector Element 21 on Array 2-159-1A	1-19
15	Histograms for Array 2-159-1A (Temperature = 193°K)	1-20
16	Detector Responsivity Histogram (Array 2-159-1A, Temperature = 193°K)	1-20
17	Detector Noise Spectral (Array 2-159-1A, Temperature = 193°K, Element 21)	1-21

LIST OF ILLUSTRATIONS (Continued)

Figure		Page
18	Detector Lifetime Versus Bias (Array 2-159-1A, Element 4, Temperature = 193°K)	1-22
19	Cross Section of the Epi Bipolar Showing Possible Leakage Paths	1-25
20	Configuration of the Epi Bipolar Transistor Design	1-26
21	Theoretical and Experimental Aperture Corrector Response	1-27
22	Aperture Corrector Impulse Response	1-28
23	Theoretical and Experimental Phase Response	1-28

1.0 INTRODUCTION

Upon conclusion of Phase I of the Thermal Weapon Sight contract, several added areas which required additional design and analysis were identified. To address these items a six month extension of the TWS program was negotiated. This additional effort was to provide further insight into system design tradeoffs and would answer several important questions not addressed in Phase I. The ^{Thermal Weapon Sight} (TWS) Phase I extension concentrated on the analysis of the following two main areas: (a) opto-mechanical design - and (b) two-line PC HgCdTe MFPA test and evaluation.

I. PHASE I EXTENSION IR OPTICAL DESIGN ACTIVITIES SUMMARY

During the Phase I add-on period, the following items were evaluated for optical and opto-mechanical implications:

1. IR Telescope, *Infrared*
2. IR Imager,
3. System Performance Trade-offs,
4. Coating Requirements, *and*
5. Display Optics.

The IR Telescope Configuration

A six element afocal telescope was selected as a baseline design configuration to evaluate a design consisting of four elements. This design, when compared to the six element configuration, revealed severe performance losses. These losses occurred at the edge of the instantaneous field of view, represented by the edge detectors in the array. The four element design was thus abandoned.

Figure 1 shows utilization of two elements between the front lens group and the eyepiece lens group. This configuration resulted in a very flat field and consequently a high average response for all detectors in the array.

The study also revealed another characteristic of the basic design concept. Two front elements are required to provide proper spectral correction over the specified spectral range. Substituting alternate materials did not improve the spectral correction of a single front element configuration, shown in Figure 2, to a level competitive with any doublet configuration evaluated earlier. Performance data are shown in Figure 3.

The IR Imager Configuration

The purpose of the IR imager, shown in Figure 4a, is two-fold. Its primary purpose is to focus collimated energy reflected off the scan wheel on the detector array. The second purpose is to control the amount of energy reaching the detectors and to provide even irradiance over the entire detector array as shown in Figure 4b. An aperture stop, located in the space between the detectors and the rear element limits the energy to an F/cone of 1.45. The energy loss for off axis detectors results from

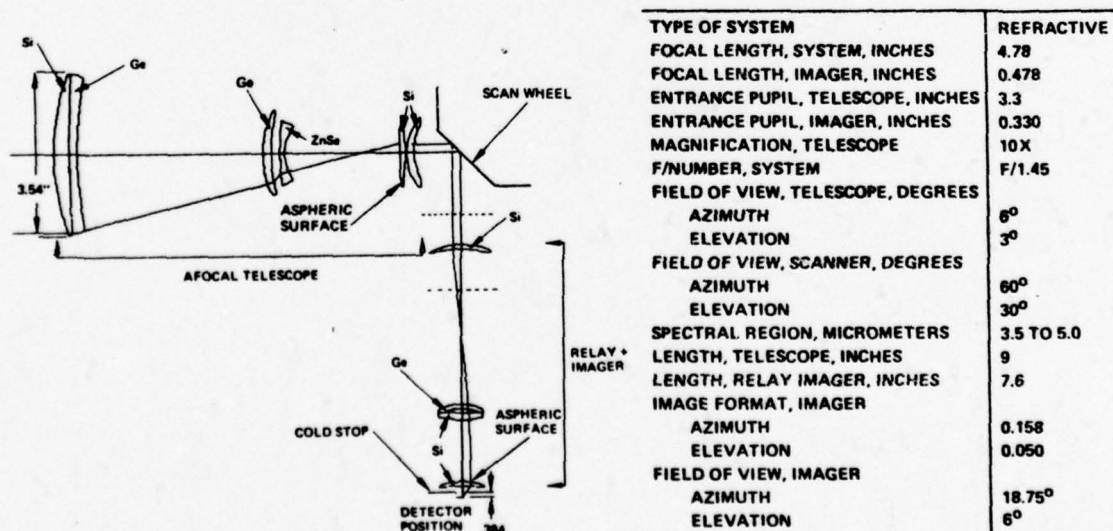


Figure 1. Optical layout of baseline TWS FLIR design.

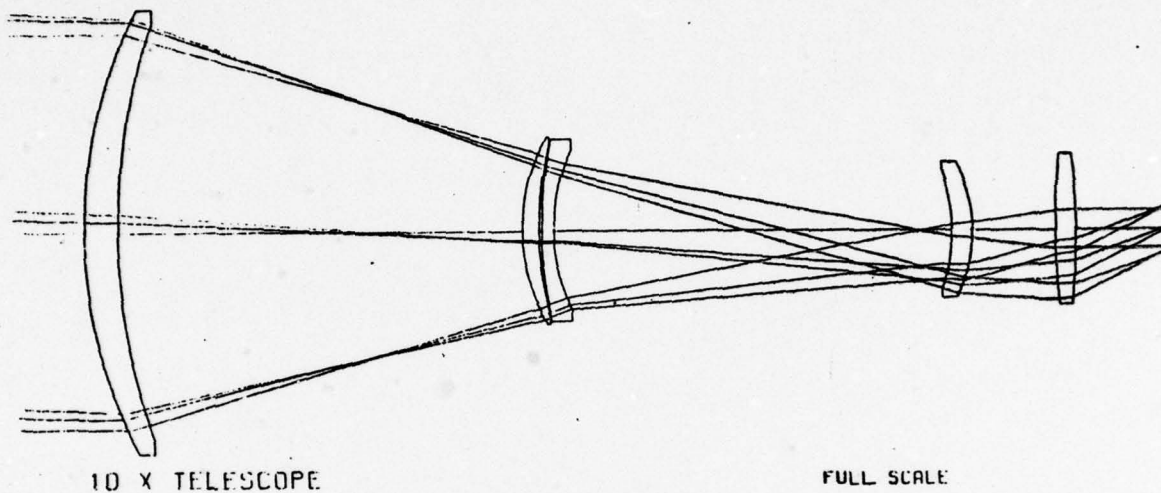


Figure 2. TWS FLIR afocal telescope optical layout.

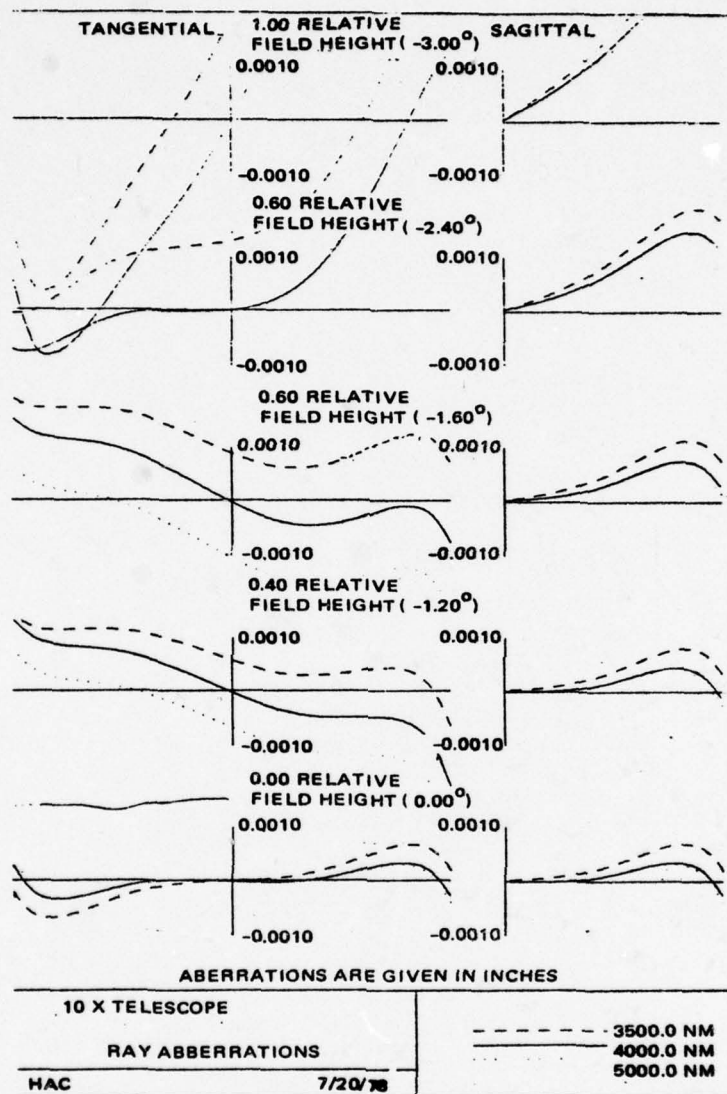


Figure 3. Performance data.

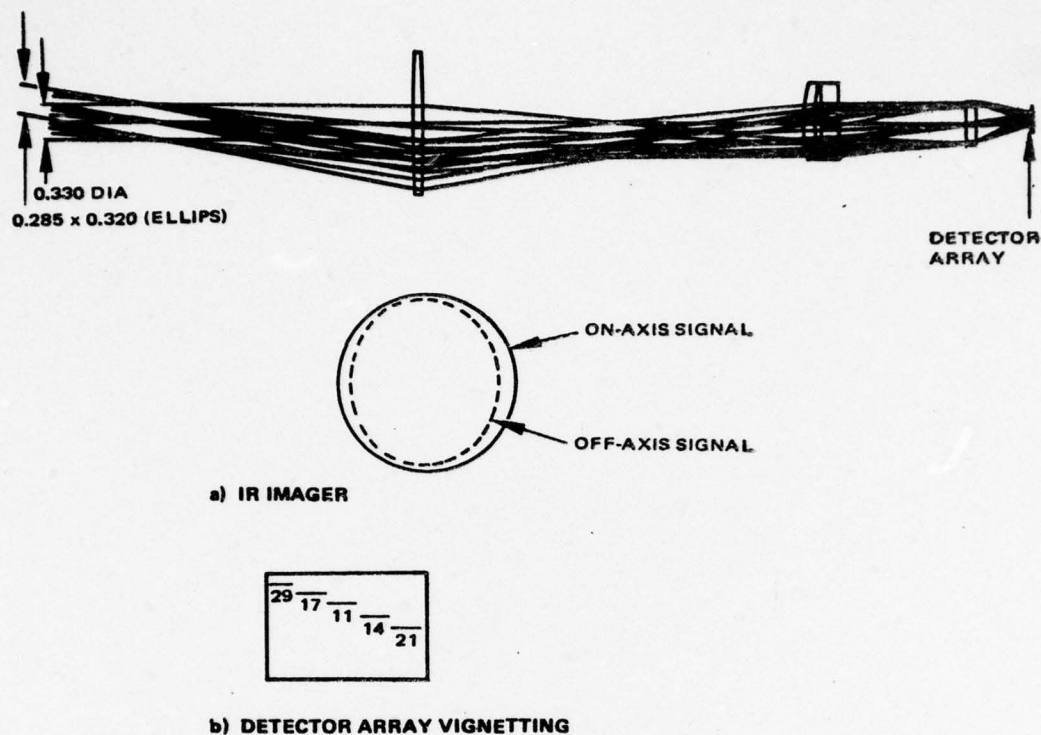


Figure 4. FLIR imager optical layout.

\cos^4 effect shown in Figure 5. To minimize the \cos^4 effect, an alternate imager configuration was designed. This design was configured to achieve a large distance between the rear element and the detectors, thus resulting in \cos^4 losses less than 5.4 percent at the extreme edges of the array.

TWS IR Optics Performance Tradeoffs

Because of the complexity of the scanner configuration, it is imperative that the telescope entrance pupil (front lens aperture) is imaged at the facet of the scan wheel. The angles of incidence at the scan wheel are so large, that under extreme conditions the incident energy is reflected at an angle of 30° with respect to the optical axis.

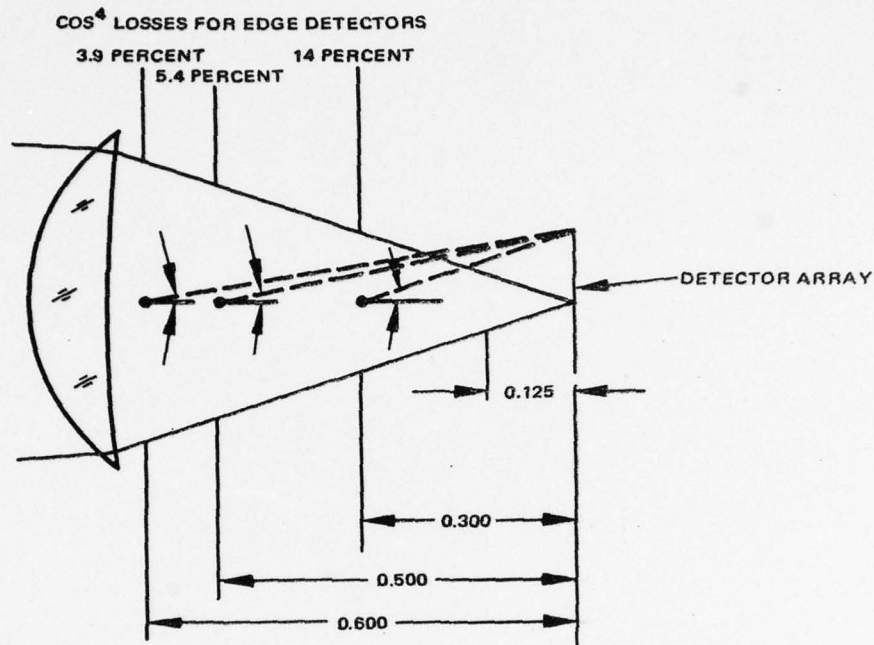


Figure 5. COS^4 losses in detector scale.

The requirements to support large angles in scanner space result in a severe performance limitation of the afocal telescope design. To analyze alternate system concepts three different optical configurations were designed as an added scope to the initialize design task. Two configurations containing an 8X and a 9X afocal telescope, respectively, were matched with appropriate imager designs to provide for an overall focal length of 4.8 inches and a 3.3 inch entrance pupil.

The results can be summarized as follows. The performance of the IR imager can be maintained at the same level as the 10X telescope system configuration. For an 8X afocal telescope design and equivalent imager design, the aspheric surface contour on one of the surfaces becomes less complex and, therefore, less sensitive to contour and centering in the optical system. The average MTF response over the array remained about the same, within 5 percent as shown in Figure 6.

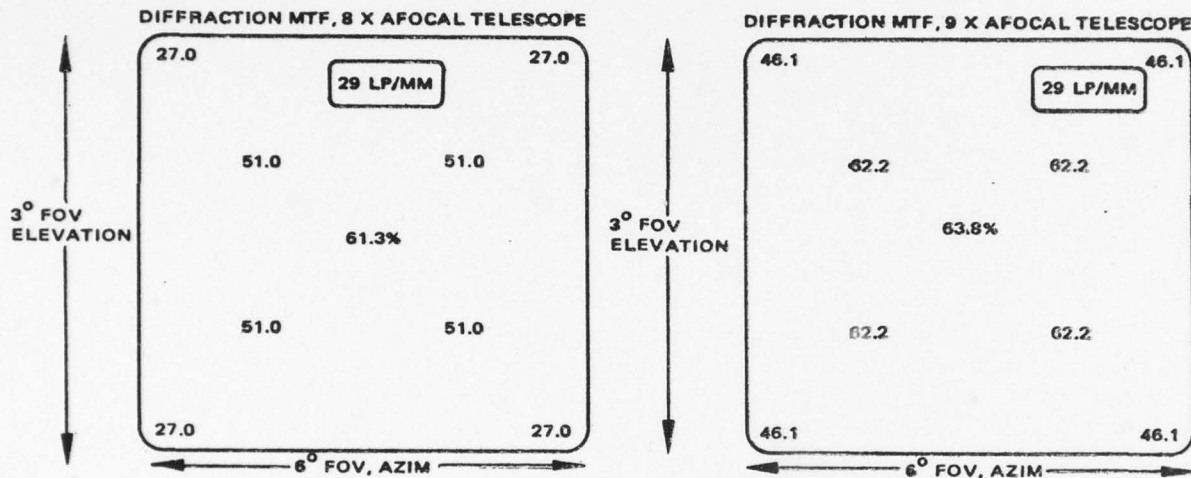


Figure 6. TWS FLIR afocal telescopes performance data for 8x and 9x afocal magnifications.

The afocal telescope designs for 8x and 9x were not subjected to the large angles in scanner space and, consequently, the performance over the field of view improved. Also, the front lens aperture could be less than what is required for a 10x design. The weight impact of the larger eyepiece lenses would probably offset the weight reduction as a result of a smaller front lens group.

One disadvantage of having a smaller lens group is that because of the change in telescope magnification, the MTF response of an 8x telescope must be 20 percent higher than for a 10x configuration. Meeting this requirement is very doubtful. The current average of 64 percent (the extremes are 73 and 49 percent) must be increased to 76.8 or 88 percent for the center and 59 percent for the corners of the detector array. The only way to achieve this result would be to increase the number of imager elements and/or the complexity of the aspheric elements and to meet a specification of $F/1.3$, for which a higher diffraction limited MTF value could be obtained.

Coating Requirements

The specifications for the high efficiency coating are given below:

1. Average reflectance <0.5 percent per surface
2. Average transmittance >97 percent per element
3. Wavelength region 3.5-5 μm .

The standard humidity and adhesion requirements were included to secure durability of the coating layers.

Display Optics

The initial (Phase I) display optics design did not meet the following specifications:

1. Stationary exit pupil at >1 inch.
2. Eyepupil excursions <0.120 inch to observe the full display at any scanwheel position (Figure 7).
3. Provide for a flat field at the reticle location.

To improve the display optics design, the design tasks were separated into three areas:

1. Redesign the imager to provide a stationary exit pupil at the scan wheel.
2. Optimize the focussing lens to provide a flat reticle focal plane.
3. Match the relay optical design with an eyepiece to compensate the residual aberrations of the relay lens group.

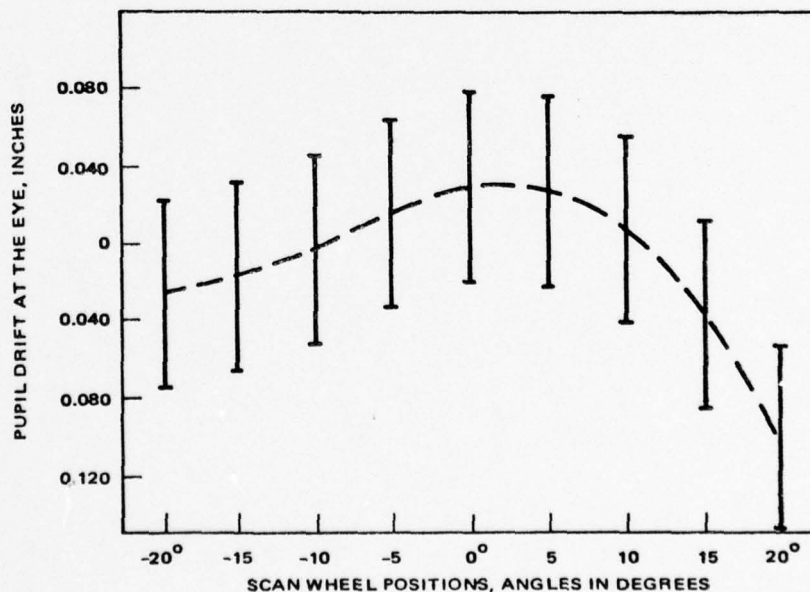


Figure 7. TWS visual display (eye pupil excursions at the exit pupil).

The resulting design provided a major improvement for the TWS visual optics design as shown in Figure 8.

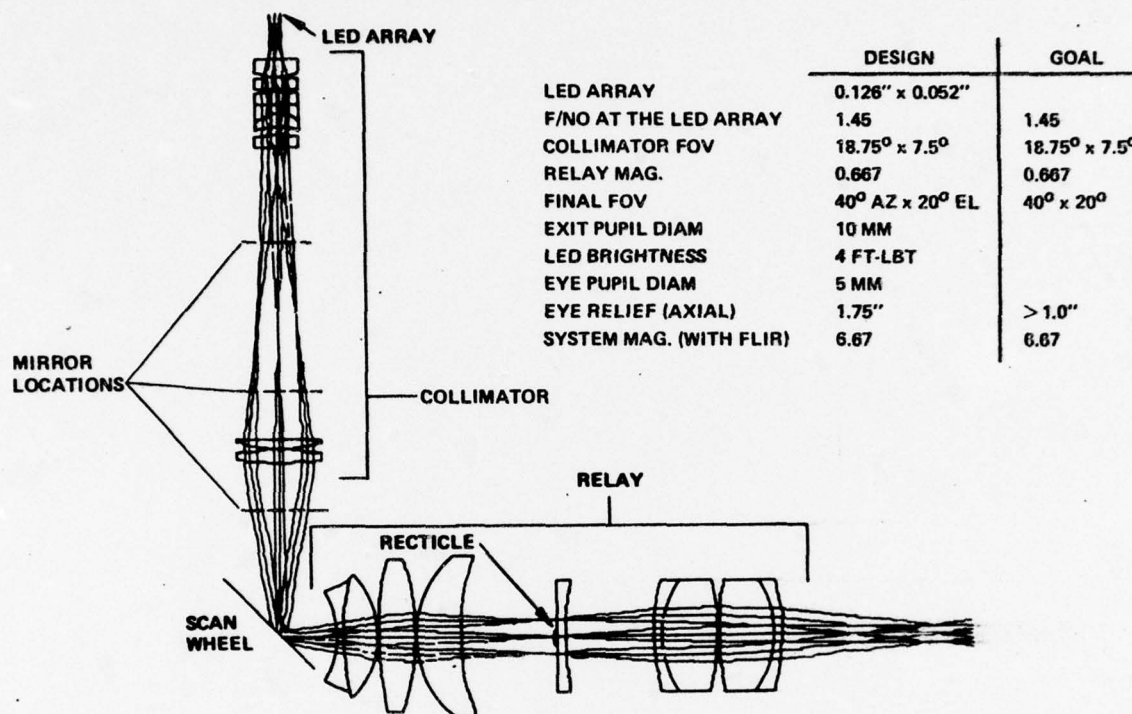


Figure 8. TWS visual system optical layout.

II. PHASE I EXTENSION MECHANICAL DESIGN ACTIVITY SUMMARY

The Phase I extension effort was directed at updating the scanner design and included an investigation into techniques that would extend the life of the elevation mirror drive cam, and an analysis of the factors which determine motor design parameters.

Elevation Mirror Drive Cam

At the conclusion of Phase I, the elevation mirror drive cam was determined to experience premature wear. The details of this analysis are included in Attachment A. A summary of the analysis is that the use of a seemingly appropriate size spherical cam follower, combined with the inherently high loads due to the required accelerations, causes excessive compressive stresses at the surface of the cam lobe. These stresses can be reduced and, hence, life increased, by enlarging the cam follower diameter or, departing from the sphere, tailoring the follower diameter and crown radius as needed. Table 1 summarizes the effect of these changes.

Enlarging the spherical diameter of the follower seems to be the desired approach, but drawbacks exist. The follower, as it gets larger, comprises a greater portion of the total inertia being accelerated by the cam. This increased inertia requires greater torque about both the mirror pivot axis and the cam axis. The result is an increase in motor torque requirements and a greater fluctuation in steady state scanner speed.

Deviating from the spherical follower also has a drawback. As discussed in Attachment A, the effective arm length would vary with changes in the mirror angle requiring a revision to the cam profile. The shape of the cam must compensate for changes in arm length. While this change adds complexity to the design task, it still appears to be a better tradeoff than increasing inertia of the oscillating elevation mirror yoke.

Table 1 shows that the crown of the cam follower must have some curvature. This curvature would not be a necessity if a spherical, or three dimensional cam was employed. The spherical cam keeps the cam surface and axis of the follower parallel during the entire cycle permitting use of a pure cylindrical follower as shown in Figure 9. The reduction in compressive stresses and sliding yields a cam life that is virtually infinite. However,

TABLE 1. EFFECT OF CAM FOLLOWER GEOMETRY ON ELEVATION
MIRROR CAM LIFE (CAM SIZE, PEAK LOAD,
AND SPEED HELD CONSTANT)

Cam Follower Dimensions (inches)		Cam Life (hours)	
Diameter	Crown Radius	No Sliding	9 Percent Sliding
0.312	Spherical	0.73	0.01
	0.250	44	1.9
	0.312	276	19.5
	0.375	1,150	116
	0.438	3,810	526
	0.500	10,300	1,840
	0.625	53,300	14,400
	0.750	187,000	69,700
0.312			
0.500	Spherical	1,380	147
	0.312	9,380	1,630
	0.375	43,700	11,200
0.500	0.438	160,000	57,200
0.625	Spherical	43,300	11,100
0.625	0.438	705,000	369,000
0.875	Spherical	5,360,000	4,700,000

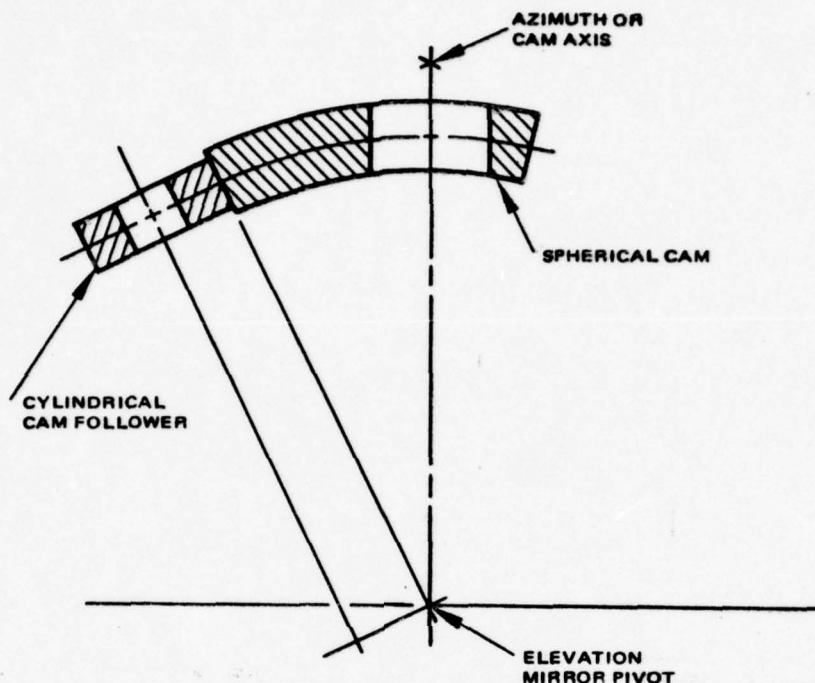


Figure 9. Spherical cam.

the fabrication costs may not warrant incorporation of this otherwise superior method.

Another technique for driving the elevation mirror is shown in Figure 10. A face type cam which is integral with the azimuth scan wheel drives a follower that is located farther from the mirror pivot. The main features of this arrangement are reduced cam loads, reduced oscillating inertia, and liberal cam profile tolerances. The chief drawback is the complexity added to the azimuth scan wheel. Additionally, before this design could warrant further consideration, an analysis of the inherent balance problem and facet deflections must be conducted.

Since cam wear is a function of load, an attempt was made to modify the cam profile to reduce peak accelerations and, hence, peak loads. As discussed in Appendix A, the cam profile is of the third harmonic type. By employing a modified trapezoidal profile peak, accelerations can be reduced 4 percent as shown in Figure 11. Whether this change can be incorporated or

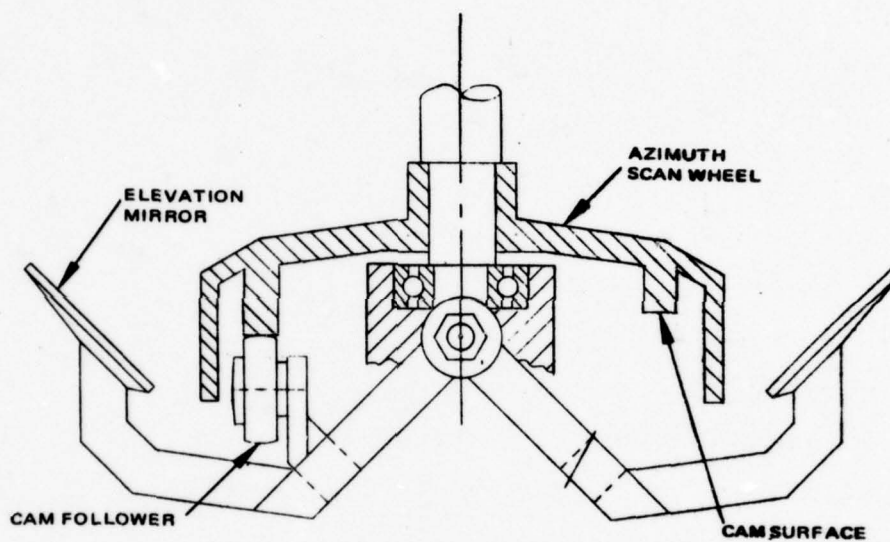


Figure 10. Elevation scan drive utilizing a face type cam.

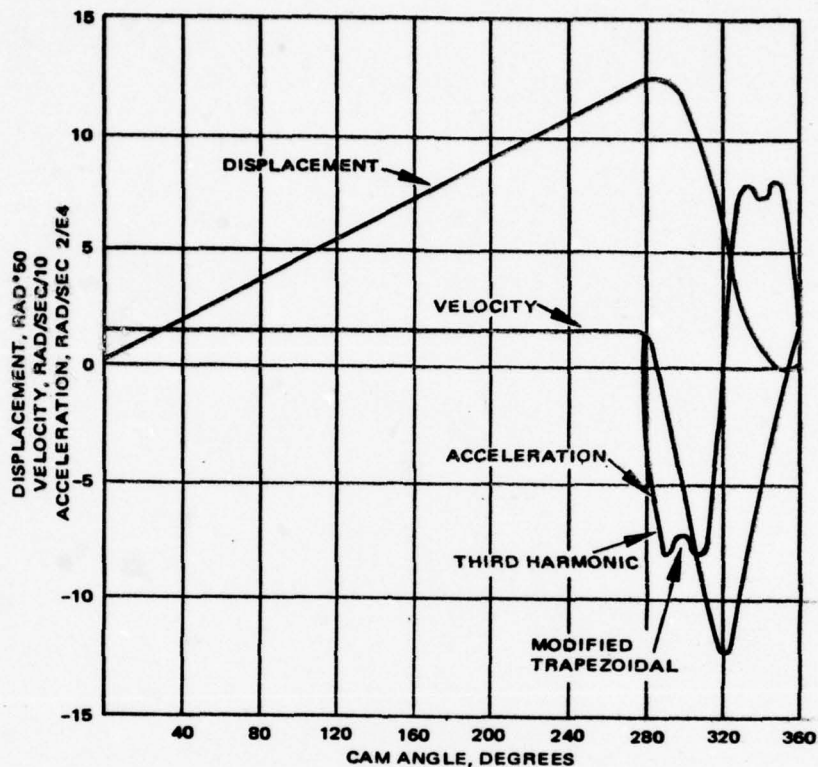


Figure 11. Elevation scan motion.

not is a function of dynamic response of the mirror yoke. The modified profile will possess a greater harmonic content, increasing the chances of exciting yoke resonances. Since a dynamic analysis of the mirror yoke is necessary regardless of which cam profile is used, the issue can readily be resolved.

Scan Motor

The scan motor requirements were discussed in Phase I and described in detail in Appendix A. Updating that analysis has been completed and motor parameters have been defined.

Figures 12 and 13 illustrate the performance of the scanner when driven by the subject motor at the minimum and maximum supply voltages of

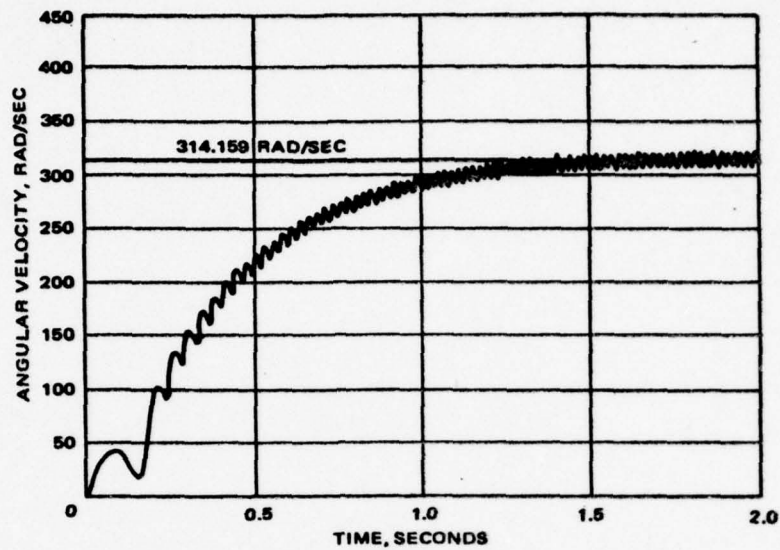


Figure 12. TWS scanner spin-up time at minimum battery voltage.

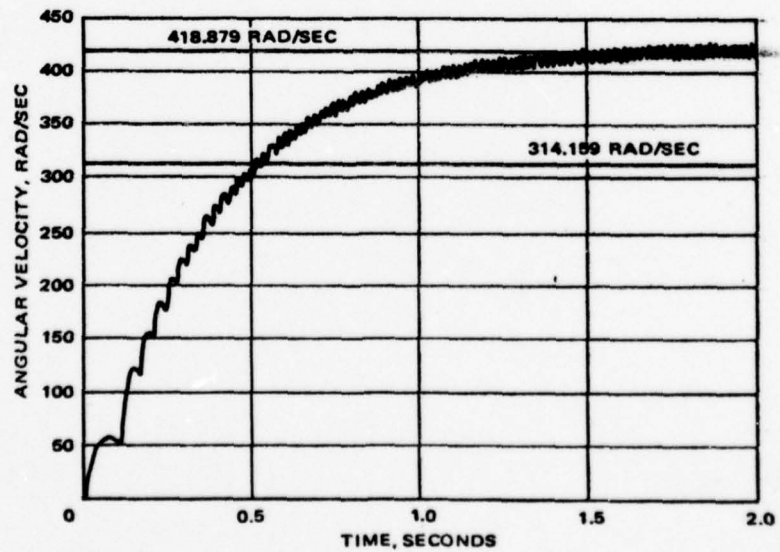


Figure 13. TWS scanner spin-up time at maximum battery voltage.

6.0 and 8.0 volts respectively. Spin-up time is approximately 2.0 seconds and steady state speed fluctuations are less than ± 3 percent for both cases.

Since the scanner must be capable of operating over the full range of battery voltage, the determining case for establishing motor performance requirements occurs when supply voltage is a minimum. At this operating point the scanner should be capable of being spun-up to the minimum allowable scan rate. This rate has been accomplished; however, when battery voltage is a maximum, the scan rate is 34 percent greater. At this speed the elevation mirror yoke is experiencing peak accelerations during the retrace cycle that are 80 percent greater than normal. The effect is a further complication in achieving acceptable cam life. Clearly, a method that will eliminate this high speed condition warrants investigation.

III. PHASE I EXTENSION MFPA ACTIVITIES

The PC HgCdTe MFPA development during the first half of 1978 was pursued through Hughes IR&D support from January 1 through April 30 and continued under the Phase I extension contract funds from May 1 through June 30, 1978.

The following efforts were undertaken during these six months:

1. Fabrication of 60-element two-line PC HgCdTe arrays on sapphire substrates.
2. Detector array tests.
3. Detector 1/f noise reduction study.
4. Layout and fabrication of the 300-element detector mask to be used with the CRC 124 chip.
5. Fabrication of CRC 124 chips.
6. CRC 124 device evaluation.
7. Bipolar process optimization.

PC HgCdTe Detector Development

Fabrication of two line arrays was continued to optimize the processing and perform further characterization. Processing has progressed to the point where 9-mil line spacings can be made routinely. The detector data obtained on two-line arrays processed are summarized in Table 2.

The best overall performance was found on array 2-159-1A which is shown in Figures 14 through 18. The spectral response measured on detector element 21 of the array is shown in Figure 14. The 50 percent cut-off wavelength is $4.7 \mu\text{m}$. Figure 15a shows a histogram of the detector resistances in which the average value of $1970 \text{ ohms} \pm 10 \text{ percent}$ for 25 elements was measured. A histogram of the $D_{\lambda p}^*$ which averaged $7.2 \times 10^{10} \text{ cm Hz}^{1/2} \text{ W}^{-1}$ is shown in Figure 15b. The best element on this array had a $D_{\lambda p}^*$ of $9.0 \times 10^{10} \text{ cm Hz}^{1/2} \text{ W}^{-1}$. The histogram for the peak responsivity is shown in Figure 16 which had an average value of $410 \times 10^3 \text{ V/W}$ at 20 V/cm bias field. The noise voltage versus frequency is plotted in Figure 17 for one element at three different bias fields. As shown, the noise is sensitive to bias voltage; however, the 1/f knee for this array is somewhat lower than that of 4-11-137 at the same bias fields. The lifetime versus bias voltage is shown in

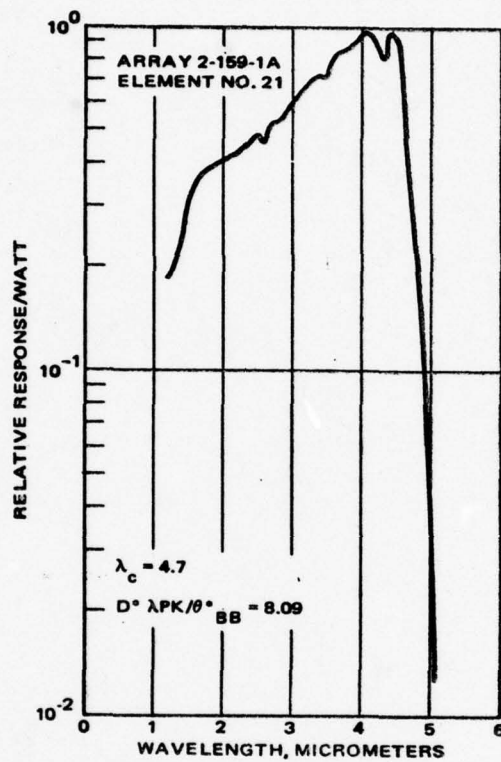
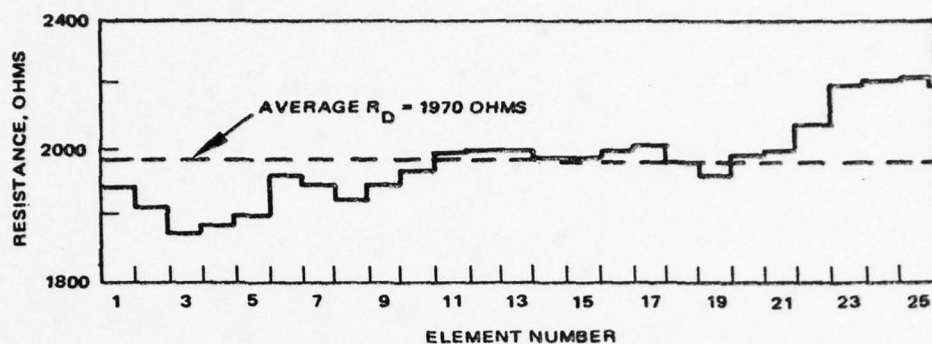


Figure 14. Relative spectral response/watt for detector element 21 on array 2-159-1A.

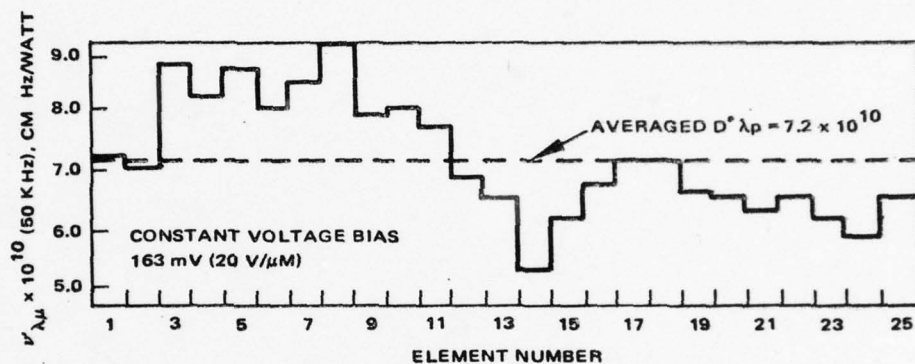
TABLE 2. TWO LINE ARRAY DATA

Array Number	Lot Number	Number of Elements Tested	Average Cold Resistance, Ohms	Lifetime at Opt. Bias, μ s	Cut-off λ_c , μ	Noise Voltage at Opt. Bias, NV/Hz $1/2$	D_{AP10} (10 KHz) $\times 10^{10}$ (cm Hz $1/2$ w^{-1})	Data Corrected for Window Losses	D_{AP10} (50 KHz) $\times 10^{10}$ (cm Hz $1/2$ w^{-1})	D Max (50 KHz) $\times 10^{10}$ cm-Hz $1/2$ /w	Declination Tech.	R $\times 10^3$ V/W	1/f KHz, Hz
4-11-95	4	30	1111	-	4.7	8.4	3.5	Yes	-	-	IB + CE	115	5K
2-144	5	7	729	-	-	-	-	-	-	-	IB + CE	-	-
4-11-100	6	13	400	-	5.0	7.2	5.5	Yes	-	-	IB + CE	104	2K \rightarrow 3K
2-152-3H	8	5	2130	.2 \rightarrow .3	4.7	12.6 \pm 50 13.4 KHz	5.3	Yes	6.6	8.6	CE	346	10K \rightarrow 50K
2-152-4F	8	14	800 \rightarrow 2300	-	-	-	-	-	-	-	CE	-	-
4-11-136	9	30	1700	-	-	-	-	-	-	-	CE	-	-
4-11-103	10	9	1770	.48 \rightarrow .60	4.8 calc.	9.0 μ 50 KHz	3.3	Yes	5.1	-	CE	226	10K \rightarrow 15K
4-11-137	10	14	1220	.3 \rightarrow .9	4.8 calc.	11.0 μ 50 KHz	3.2	Yes	5.8	7.8	CE	309	5K \rightarrow 10K at 10V/cm 20K at 30V/cm
2-168-1C	11	2	2270	.2	-	-	1.4	Yes	-	-	CE	127	-
2-168-4C	11	11	1580	.2 \rightarrow .34	-	-	1.3	Yes	-	-	CE	101	-
2-159-2C	13	11	5060	-	4.8 calc.	-	-	Yes	5.3	-	CE	747	20K
2-159-1A	13	25	1970	1.1	4.7	9.2 μ 50 KHz	4.3	Yes	7.1	9.2	CE	358	1K at 7V/cm 10K at 20V/cm

NOTE: (1) Data corrected for window loss through uncoated IR-2 window.
(2) IB = ion beam milling; CE = chemical etching.



a) DETECTOR RESISTANCE



b) DETECTOR D^*

Figure 15. Histograms for array 2-159-1A (temperature = 193°K)

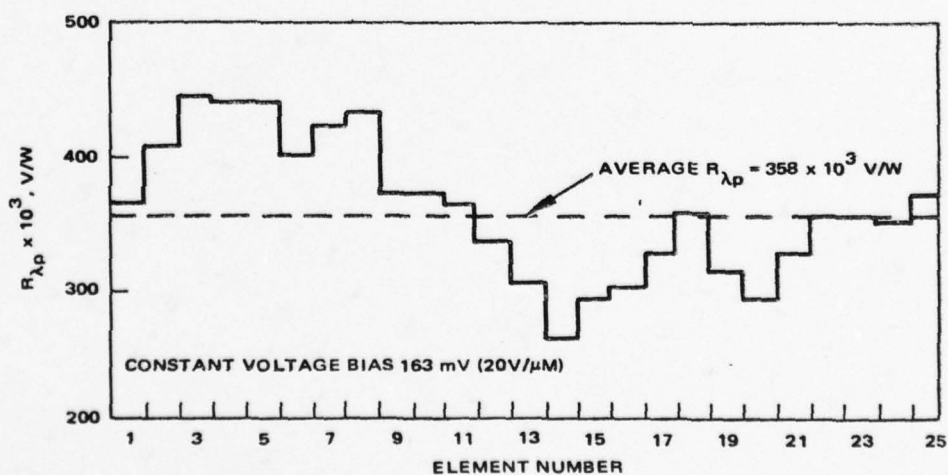


Figure 16. Detector responsivity histogram (array 2-159-1A, temperature = 193°K).

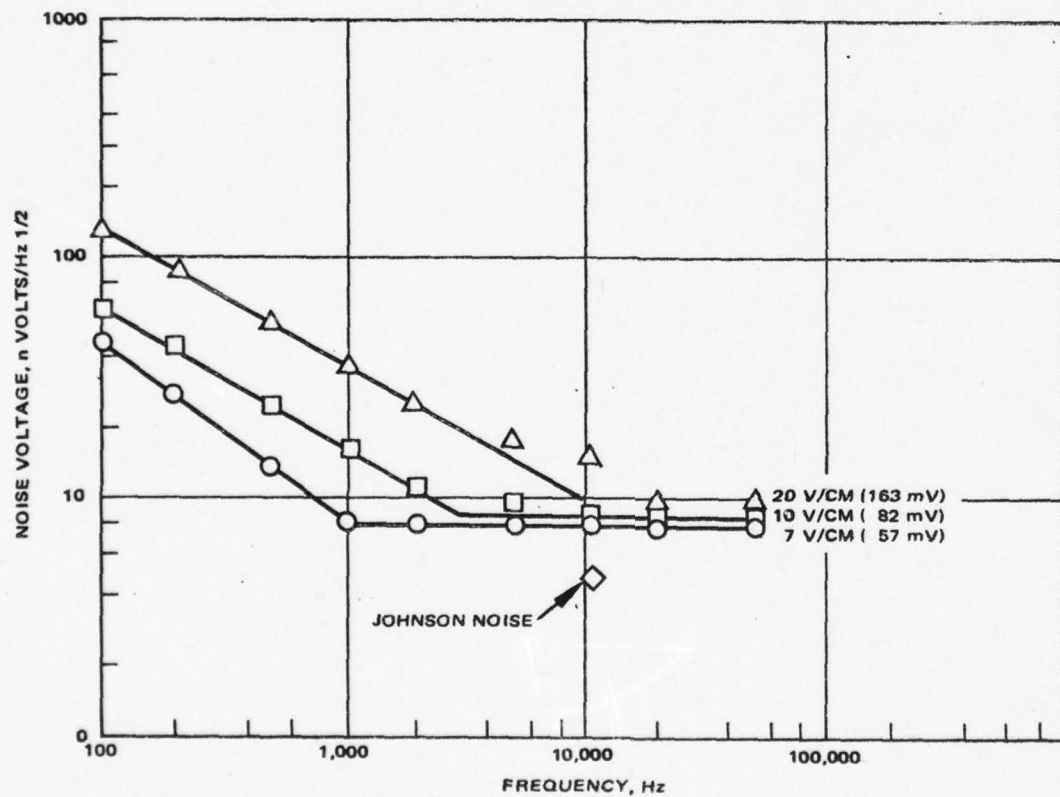


Figure 17. Detector noise spectral (array 2-159-1A, temperature = 193°K , element 21)

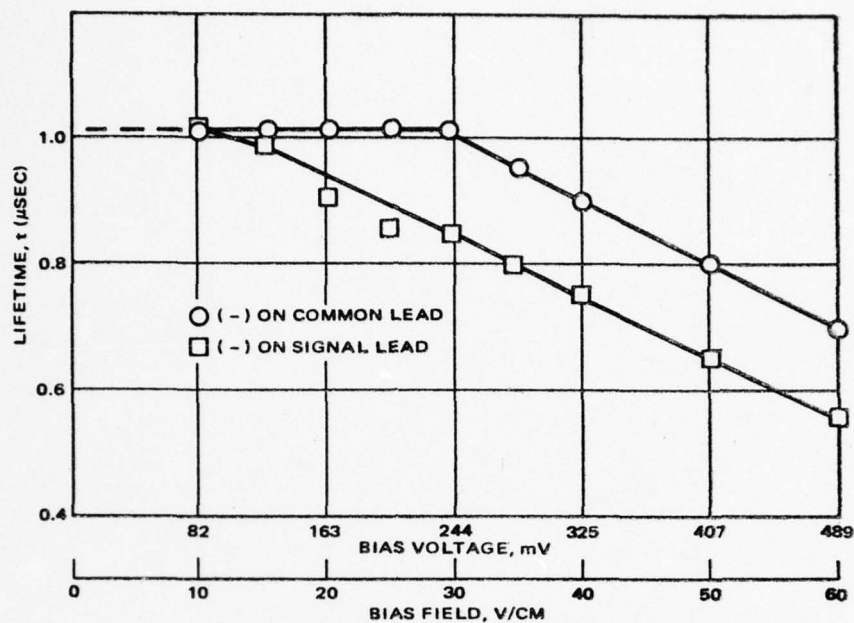


Figure 18. Detector lifetime versus bias (array 2-159-1A, element 4, temperature = 193°K).

Figure 18. This array has the longest lifetime of 1.1 μ s for the two-line arrays fabricated to date. The TWS Phase I predicted a sweep-out limited lifetime of 0.7 to 1 μ s which has been achieved with the processing techniques utilizing the chemical etching approach.

Certain detector parameters listed as important goals in the TWS Phase I proposal are reiterated in Table 3. Array 2-159-1A meets these goals for detector resistance, detector power dissipation, lifetime, and noise. The $D_{\lambda p}^*$ for this array is still below the desired value of 1×10^{11} ; however, at least one element is 92 percent of the goal with the average value of 71 percent of the goal.

TABLE 3. TWO LINE (9 MIL SPACING) DETECTOR ARRAY
PERFORMANCE VERSUS TWS PHASE I
REQUIREMENTS

Parameter	TWS Phase I Requirements	Array 2-159-1A (Lot 13)
$D_{\lambda p}^*$ (avg.), $\text{cm Hz}^{1/2} \text{ w}^{-1}$	1×10^{11}	7.1×10^{10}
$D_{\lambda p}^*$ (max), $\text{cm Hz}^{1/2} \text{ w}^{-1}$	—	9.2×10^{10}
Noise, $\text{nV/Hz}^{1/2}$ at 50 kHz frequency	≥ 7.5	9.4
Johnson noise, $\text{nV/Hz}^{1/2}$	≥ 3.2	4.6
Temperature, $^{\circ}\text{K}$	195	Freon 13 (193)
Resistance, ohms	≥ 1000	1970
Optimum bias voltage, mV	—	163
Detector power dissipation, μW	15	13.5
Lifetime at optimum bias τ , μs	0.7 to 1	1.1

PC HgCdTe DETECTIVITY IMPROVEMENT EFFORT

During the first phase of the TWS program, several two-line arrays have been produced without achieving the goal detectivity of 1×10^{11} at 195°K . This effort has continued under the interim 1978 IR&D funding, and is approaching the problem from several directions.

The problems which have presently limited array detectivity and their potential solutions are listed in Table 4.

The emphasis on lots processed was focused on the $1/f$ noise problem. Several experiments had been configured and lots processed to optimize the contacts for lowest $1/f$ noise at the proper detector bias.

Layout of the 300-detector element (CRC 124) mask was completed at Santa Barbara Research Center (SBRC). Masks were fabricated at Electro-mask and delivered to Santa Barbara. Detector layout of the first five rows allow compatibility with an imaging demonstration using the 124-chip.

TABLE 4. ARRAY DETECTIVITY PROBLEMS AND SOLUTIONS

Identified Problem	Solution
1. Excess Noise ($1/f$ noise)	Improve contact metallization scheme.
2. Low Quantum Efficiency	Increase optical absorption. Reflective back surface.
3. Thermally limited	Maximize bulk lifetime. Maximize contact expansion.
4. Johnson Noise Limited ~6 percent	Increase sweepout limited responsivity by improved ambipolar mobility.

Processing of the first several lots with the new detector mask on scrap CRC 124 wafers to check out the detector masks and processing are planned for the beginning of TWS Phase II contract effort.

CRC 124 Chip Processing and Testing

Processing of the CRC 124 has continued at Carlsbad. Processing of two lots of 124 chips have been completed and measurements were made on the bipolar and MOS test translators. Some of the important bipolar parameters (measured on the 124-3 lot) are summarized in Table 5. A problem involving the isolation breakdown of the base, and measurements revealed a resistive path, or short, for the device with a 0.275 mil base to isolation spacing. Also, the device with a 0.400 mil base to isolation spacing is resistive at low voltage and has a "walking" breakdown at a higher voltage (i. e., the breakdown voltage increases with increasing applied voltage). The β of the devices is lower than desired, because of leakage from the base caused by a short to the substrate.

When the substrate is grounded there is little collector current until V_{CE} is about 2.5 to 3.0-V. With the substrate not grounded, more normal operation was observed, although some leakage still persisted.

TABLE 5. BIPOLAR MEASUREMENTS ON CRC 124-3 LOT

Parameter	Bipolar Base to Isolation Spacing	
	0.275 mil	0.400 mil
Breakdown voltage Base to Isolation	Short	Short or resistive to 3-6 V
β	1 - 2 at 100 μ A	20 - 50 at 50 μ A
Breakdown $B V_{CEO} \approx B V_{CBO}$	30 - 35 V	
$B V_{EBO}$	5.6 - 6.0 V	
Base Resistance	187 - 210 Ω/\square	

A cross section of the bipolar transistor is shown in Figure 19. The numbered arrows point to possible problem regions listed below:

1. Lateral diffusion of the p+ diffusion from isolation to base was causing a short or low breakdown voltage.
2. "P-Ghost", or unwanted P-doped layer, in the N-epi layer caused by autodoping during epi growth, which resulted in a resistive path or J-FET type of parasitic between PBL and p+.
3. Shorting of the p+ to the substrate because the NBL does not extend below the p+ in the base region and caused a short from the base to the isolation.

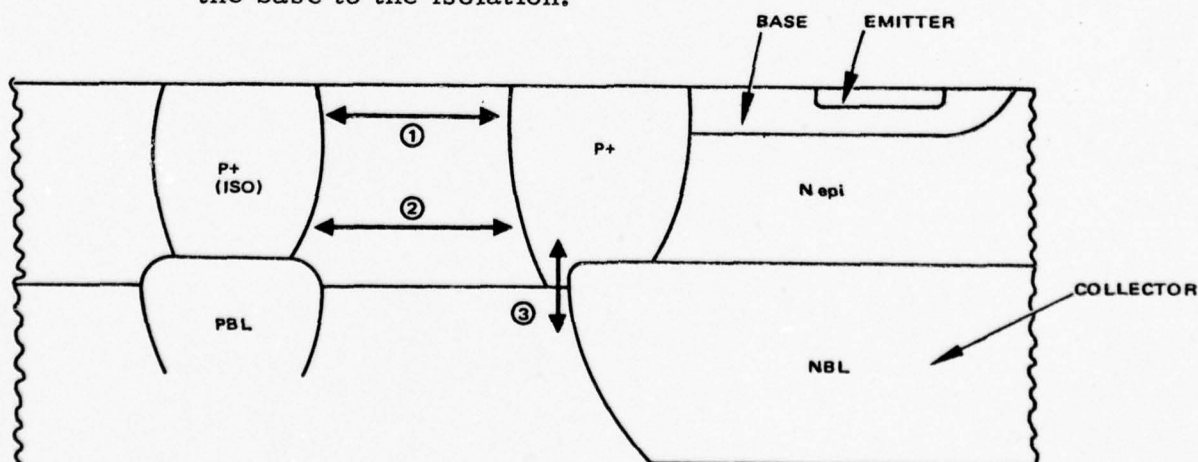


Figure 19. Cross section of the epi bipolar showing possible leakage paths.

Solutions and conclusions for the three previously mentioned problems are given below:

1. Investigation with MOS test devices showed that problem one did not exist. However, the epi bipolar was redesigned to have a larger spacing between the p⁺ isolation and the base diffusion, from 0.275 to 0.325 mil, reduced to the size of the base insert. The modified layout of the TWS epi bipolar is shown in Figure 20. These changes have been implemented into masks used for Lots 4, 5, and 6.
2. The autodoping problems were verified by spreading resistance measurements. Changes have been made in the later lots to correct the autodoping problem.
3. Reduction of the p⁺ base insert eliminated the portion of p⁺ that extends over the edge of the NBL, as shown in Figure 19.

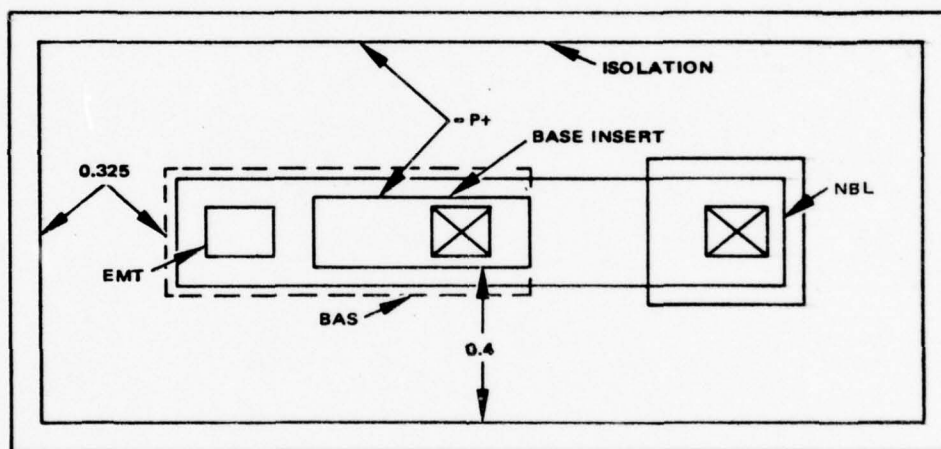


Figure 20. Configuration of the epi bipolar transistor design.

Conclusions show that the undesirable bipolar device characteristics resulted from two causes:

1. Autodoping of the PBL during epi growth which caused a p-doped layer in the N-epi.
2. Shorting of the p⁺ to the substrate where the N⁺ buried layer did not extend completely under the p⁺ (base insert) diffusion.

These conclusions are based on results obtained from measuring test device characteristics on a curve tracer.

The following changes have been implemented to remedy the situation:

1. Epi process was changed to prevent autodoping.
2. The p⁺ mask has changed to produce the p⁺ (base insert) dimension so that the NBL is under the base insert.
3. The p⁺ mask dimensions were reduced to minimize the possibility of vertical or lateral parasitic transistor action.
4. Development of a new process to eliminate the PBL was initiated.

Measurements were also made on the CRC 124 aperture corrector. The results have shown a frequency response very close to the predicted response.

The actual measured output voltage as a function of frequency is shown in Figure 21. The calculated response of the aperture corrector is $(1 - 1/2 \cos 4x) \sin x/x$. The theoretical curve, normalized to the measured data, is plotted on the same graph. The aperture corrector impulse response is shown in Figure 22. The phase response of the aperture corrector compared to theory is shown in Figure 23.

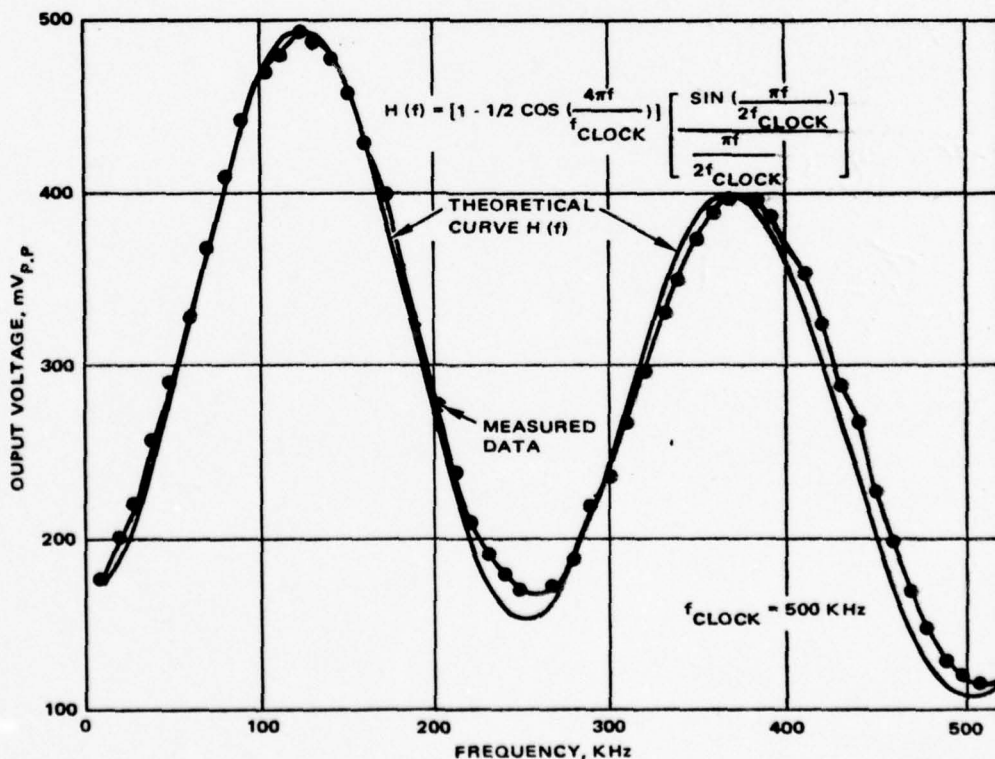


Figure 21. Theoretical and experimental aperture corrector response.

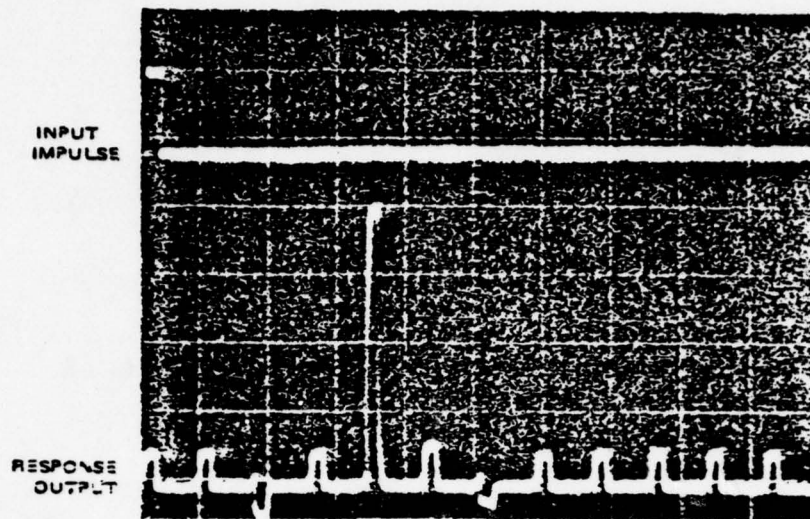


Figure 22. Aperture corrector impulse response.

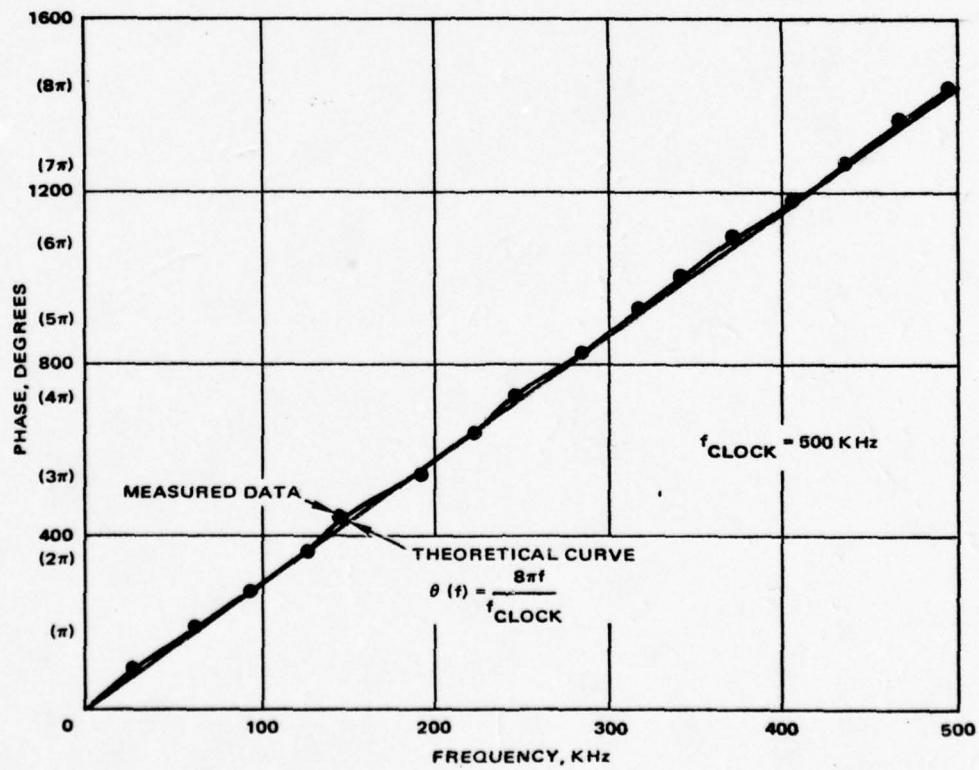


Figure 23. Theoretical and experimental phase response.

The MTF of the system will be evaluated further during the initial part of the TWS Phase II program and the proper tapping weights will be implemented to correct for the MTF roll-off. This process will make it possible to correct both the linear phase roll-off and the RC type roll-off (i. e., detector lifetime).

The aperture corrector configuration allows the MTF to be used or bypassed, so if different peaking frequency or amplitude is devised, off chip aperture correction can be implemented.

The CRC 124 has been electrically tested and has indicated that the CCD is operational. Low bipolar current gains to date have prevented testing of the detector/CCD input circuits. New lots have incorporated mask changes designed to improve the bipolar current gain.

APPENDIX A. TWS CAM DESIGN

SUMMARY

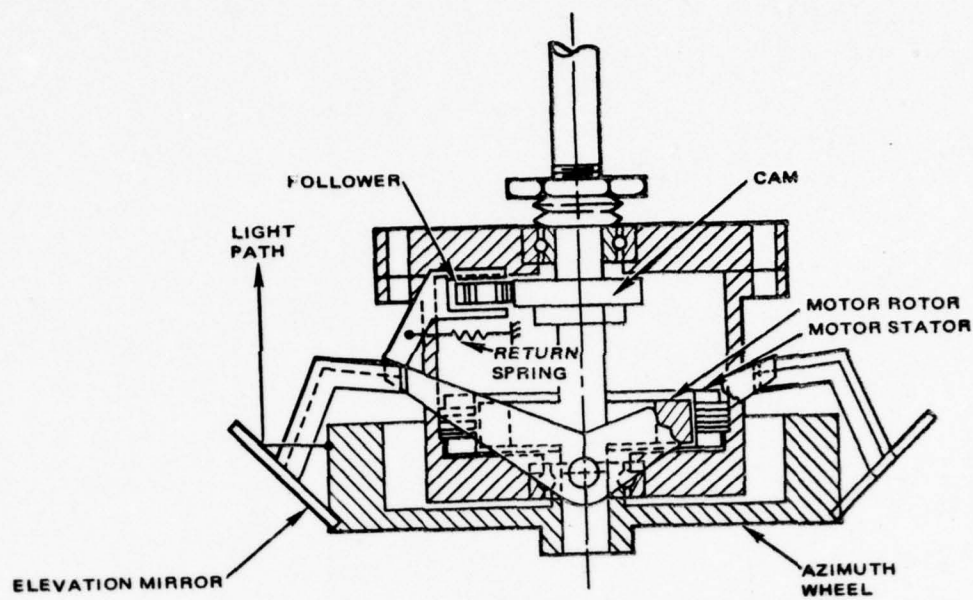
The pertinent values calculated in this analysis are given below:

Angle, Elevation Scan	13.968 degrees
Angle, Cam, During Scan	279.355 degrees
Angle, Cam, During Reset	80.645 degrees
Acceleration, Maximum Follower	$\pm 80334 \text{ radians/sec}^2$
Capacity, Follower Bearing Required Basic Dynamic	104 pounds
Displacement Follower Total	14.446 degrees
Inertia, Elevation Axis	$1.113(10^{-4}) \text{ in-lb-sec}^2$
Inertia, Azimuth Axis	$3.887(10^{-4}) \text{ in-lb-sec}^2$
Loading, Maximum Cam Normal Profile, Cam	14.3 pounds Third Harmonic
Stress, Maximum Hertz	330,423 psi
Velocity, Azimuth	50 cycles/sec
Velocity, Azimuth Delta	2.07 cycles/sec
Velocity, Maximum Follower	-124.542 radians/sec

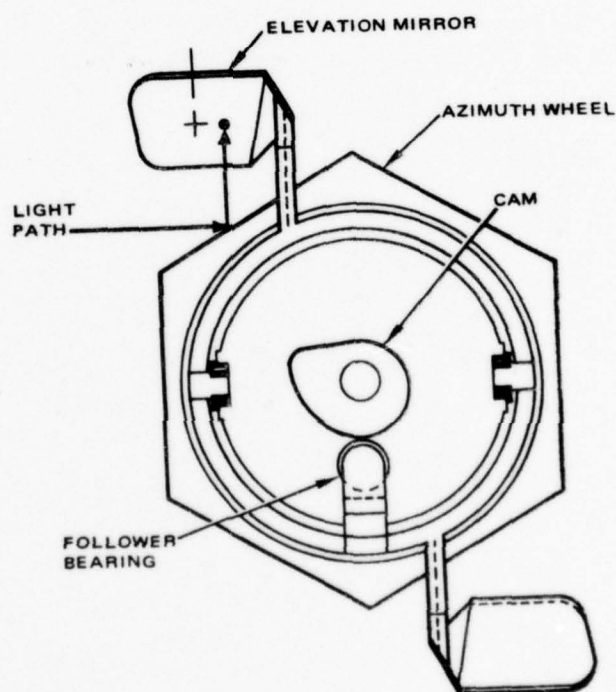
INTRODUCTION

A kinematic analysis of the TWS scanner assembly has been performed to determine motor torque requirements, cam and bearing loading, and azimuth facet-wheel speed variation.

The general layout of the scanner design is shown in Figure A-1 and the mechanical operation is described as follows. The azimuth facet-wheel, DC motor, and cam are rigidly mounted to a common shaft which turns at a constant 50 cycles/second. The elevation mirror is actuated by the cam and



a. side view



b. top view

Figure A-1. TWS scanner layout.

rotates at 13.968° at a constant scan rate during 279.355° of cam rotation and then must reset to the zero position during the remaining 80.645° of cam rotation. The elevation mirror makes one scan cycle per revolution of the azimuth wheel.

During the constant scan portion of the cycle the return spring is stretched giving it sufficient tension to keep the cam follower in contact with the cam during the high acceleration experienced during reset. This tension determines motor peak torque requirements, bearing size requirements, bearing friction losses, and the amount of energy alternately absorbed and replaced into the system causing speed variations.

CAM PROFILE

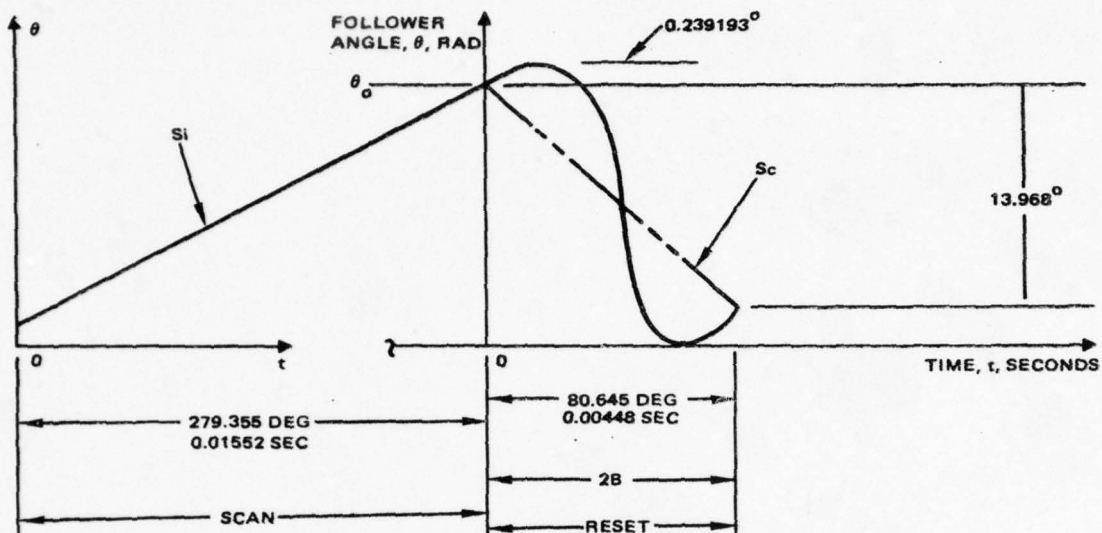
The primary requirements of a high speed cam are that it should have a low peak acceleration and, therefore, low forces, and it should not induce vibrations into the follower system. Since these two requirements are contradictory, the selected profile must be a compromise.

The cam profile used on TWS, commonly known as the third harmonic profile (Reference A-1), is a compromise between a parabolic profile (constant acceleration) which has the lowest possible acceleration, and the cycloidal profile which is the smoothest operating high speed profile. A graph of the displacement function, along with the equations of motion are shown in Figure A-2. These equations, with the appropriate values substituted, are plotted in Figure A-3.

SPRING DESIGN

The function of the return spring is to keep the follower in contact with the cam and to overcome all forces that separate the follower from the cam. These forces include inertia, windage, friction, gravity, etc. The maximum windage can be estimated from

$$\begin{aligned}\text{Drag} &= C_D \frac{\rho V^2}{2} A = (2)(0.00238)(15.625^2)(0.00283)/2 \\ &= 1.64 \times 10^{-3} \text{ pounds per mirror}\end{aligned}$$



DURING RESET

1. DISPLACEMENT $= \theta = S_c t + \frac{S_k B}{\pi} \left(0.934 \sin \frac{\pi t}{B} + 0.022 \sin \frac{3\pi t}{B} \right) + \theta_0$
2. VELOCITY $= \frac{d\theta}{dt} = S_c + S_k \left(0.934 \cos \frac{\pi t}{B} + 0.066 \cos \frac{3\pi t}{B} \right) \frac{\text{RAD}}{\text{SEC}}$
3. ACCELERATION $= \frac{d^2\theta}{dt^2} = -\frac{S_k \pi}{B} \left(0.934 \sin \frac{\pi t}{B} + 0.198 \sin \frac{3\pi t}{B} \right) \frac{\text{RAD}}{\text{SEC}^2}$
4. MAXIMUM ACCELERATION $= \pm 0.8169 S_k \frac{\pi}{B}$

WHERE,

$$S_k = S_i - S_c$$

DURING SCAN

1. $\theta = 15.707925 t + 0.0041747 \text{ RAD}$
2. $V = 15.707925 \text{ RAD/SEC}$
3. $A = 0 \text{ RAD/SEC}^2$

Figure A-2. Third harmonic profile.

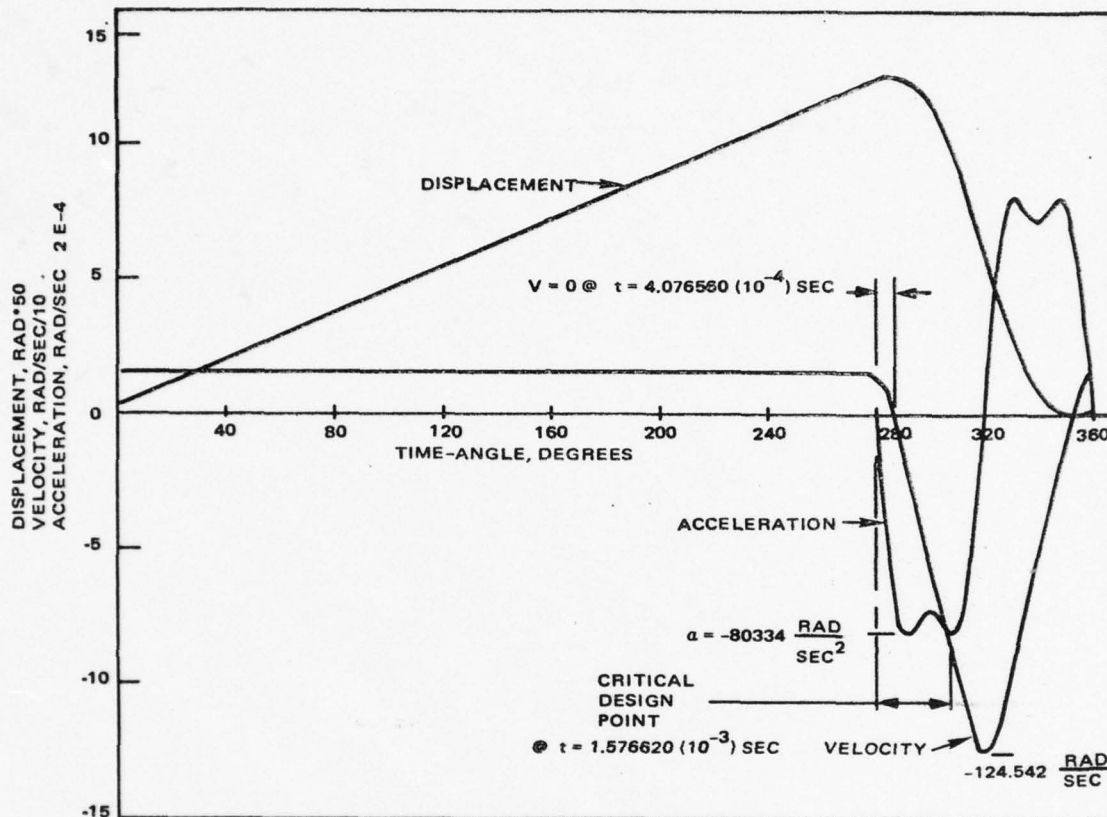


Figure A-3. TWS elevation mirror.

which corresponds to only $5.25(10^{-3})$ in-lbs which is approximately the elevation mirror axis inertia for both mirrors. Compared to the inertial loading this measurement, in addition to friction and gravitational forces, is negligible. Therefore, the only significant force which the spring must overcome is the inertia.

The critical design point for the return spring is the peak negative follower acceleration, or in the case of the third harmonic profile, the two points of peak negative acceleration. The spring must have enough tension at this point to keep the follower in contact with the cam. If the follower jump occurs it will result in noise, vibration, and rapid wear of the cam and

follower surfaces. Figure A-4 shows the inertial loading as a function of the cam angle. The inertial loading was obtained from

$$T = I\alpha$$

where

I = elevation mirror inertia about pivot axis = 1.113×10^{-4} in-lb-sec².

α = elevation mirror angular acceleration from Figure A-2, equation 3.

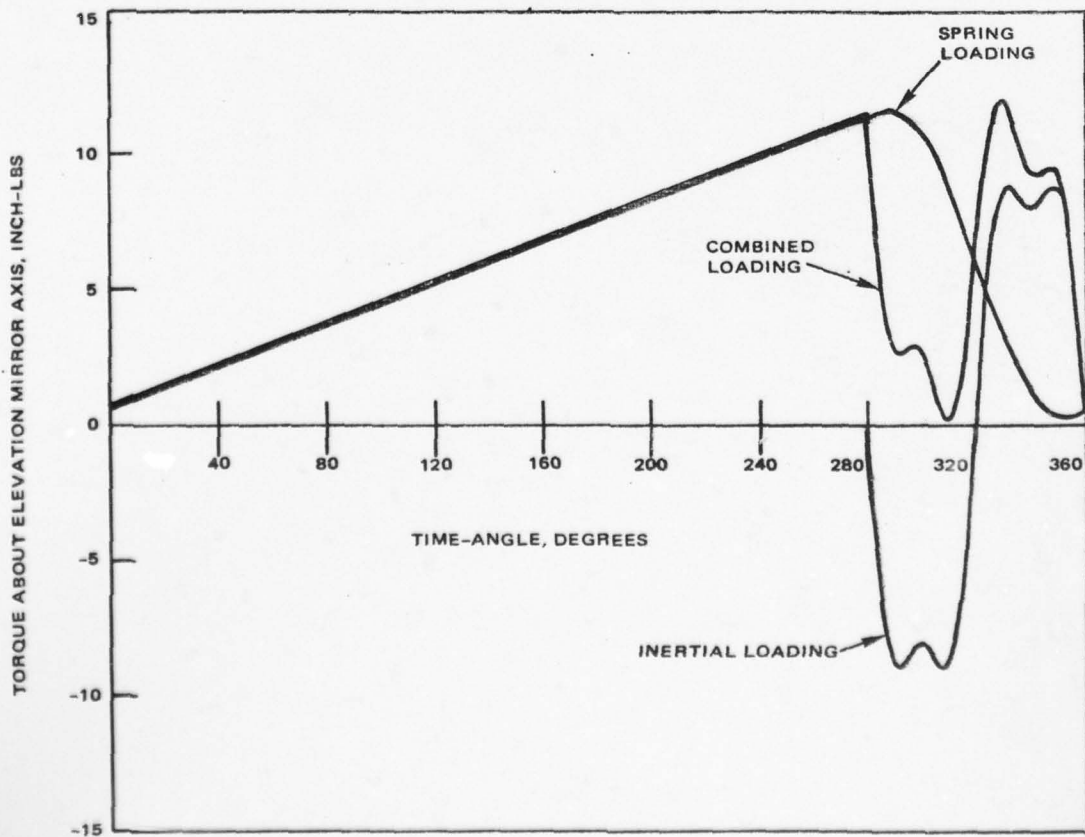


Figure A-4. TWS cam loading.

The elevation mirror inertia was obtained using the preliminary design shown in Figure A-1.

The peak negative acceleration is -80334 rad/sec^2 . The required spring torque at this point is

$$T = I \alpha = 1.113 (10^{-4})(80,334) = 8.941 \text{ in-lbs}$$

A 5 percent margin of safety of 0.447 in-lbs is assumed to compensate for friction and variations in inertia giving

$$T = 0.447 + 8.941 = 9.388 \text{ in-lbs}$$

The follower displacement at the second point of peak acceleration was calculated using an iterative solution of 11.459° . Assuming a 5 percent preload of 0.447 in-lbs the spring rate is calculated from

$$K = \frac{\Delta T}{\Delta \theta} = \frac{9.388 - 0.477}{11.459 \left(\frac{\pi}{180} \right)} = 44.7 \text{ in-lbs/radian}$$

The spring torque as a function of displacement is

$$F_S = 44.7 \theta + 0.447 \text{ in-lbs}$$

where:

θ = follower displacement from Figure A-2, equation 2.

The use of a return spring is a rather inefficient method of holding the follower in contact with the cam because the peak required spring force, for the third harmonic profile, does not occur at the maximum follower displacement. Therefore, when the follower moves to the maximum displacement the spring is stretched unnecessarily to an increased tension. This action increases the required torque of the motor and causes unnecessary friction losses.

The ratio of the peak spring torque to that required at maximum acceleration is

$$\frac{44.7 (14.445 \pi/180) + 0.447}{44.7 (11.459 \pi/180) + 0.447} = \frac{11.717}{9.387} = 1.248$$

or 25 percent more than optimum.

CAM NORMAL FORCES

The forces acting normal to the cam surface determine the surface stresses and, hence, the life of the cam and follower bearing surfaces. The equation for calculation is

$$F = \frac{T}{r \cos \phi}$$

where:

F = force normal to cam surface, pounds

T = required torque about elevation mirror pivot axis.

r = lever arm.

ϕ = pressure angle.

F , r and ϕ versus cam angle are shown in Figure A-5.

The lever arm and pressure angle are determined from Figure A-6 and the following equations:

α = cam angle

$R = 1.1271 \sin (\theta + \theta_o)$

θ = follower displacement from Figure A-2, equation 2

$r = 1.1271 \cos (\theta + \theta_o)$

ϕ = pressure angle = $\text{TAN}^{-1} \{1/R \, dR/d\alpha\}$ (Reference 2)

since α is given in terms of time, t , in Figure A-2, the chain rule is applied giving

$$\phi = \text{TAN}^{-1} \{1/R \, dR/dt \, dt/d\alpha\} = \text{TAN}^{-1} [1/RW \, dR/dt]$$

w = cam angular velocity = 314.159 radians/sec

$\theta_o = 0.3685$ radians

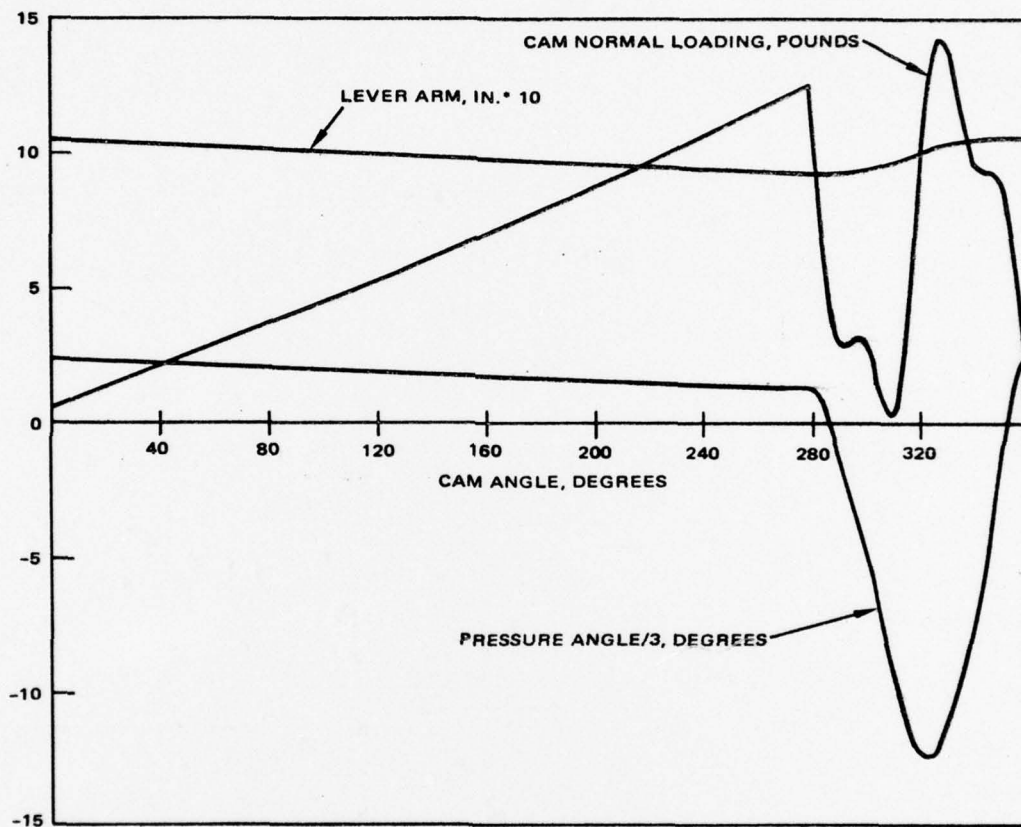


Figure A-5. TWS scanner.

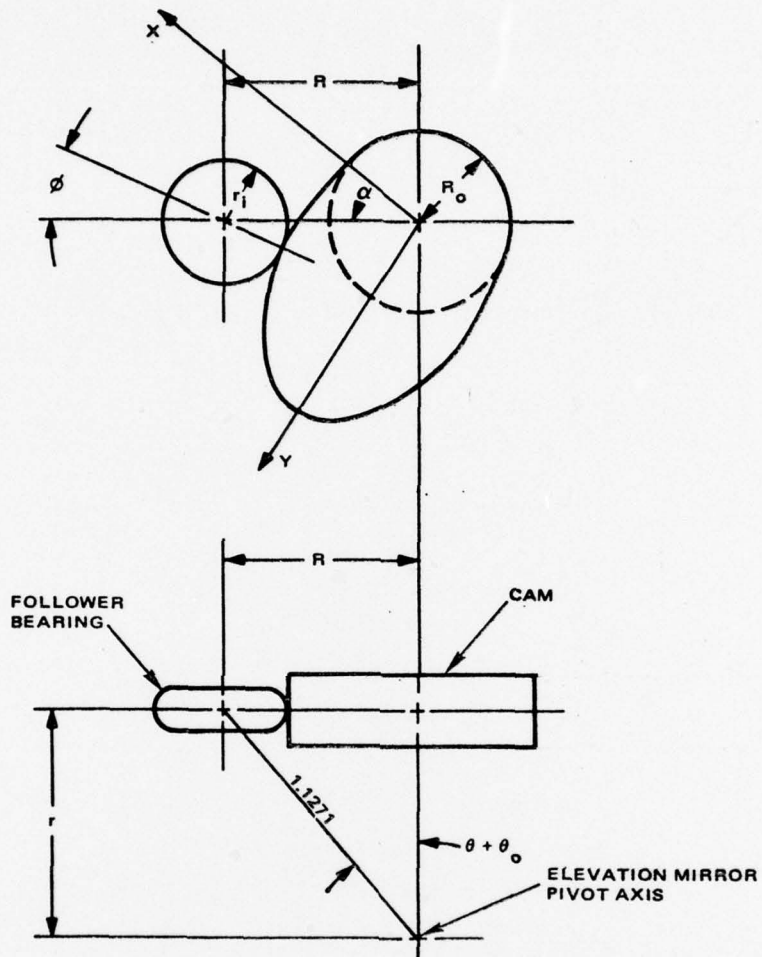


Figure A-6. Lever arm and pressure angle.

The distance of the follower bearing from the pivot axis, 1.1271 inches, and the angle θ_o were determined from the preliminary values selected for R_o , r_i , and r .

CAM PROFILE

The X and Y coordinates of the cam profile can also be determined from Figure A-6 when

$$X = R \cos (\alpha) + r_i \cos (\alpha - \phi + \pi)$$

$$Y = R \sin (\alpha) + r_i \sin (\alpha - \phi + \pi)$$

Figure A-7 shows a plot of the cam profile.

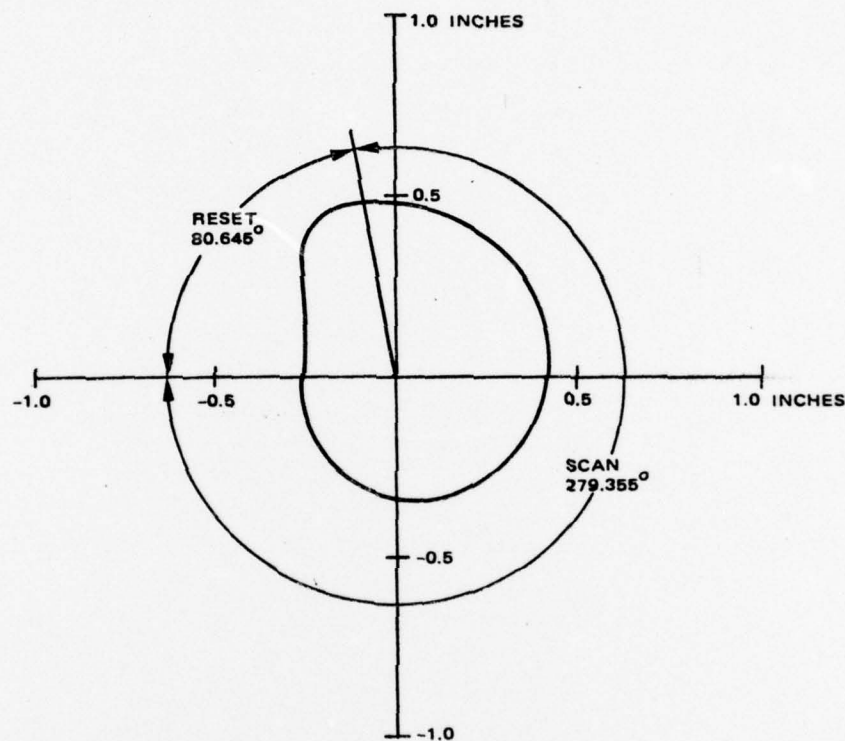


Figure A-7. Profile of TWS scanner elevation drive cam.

HERTZ STRESSES

The Hertz contact stresses were determined using the formulas given in Roark for the general case of two bodies in contact (Reference A-3). The radius of curvature of the cam surface as a function of angle has not yet been plotted for this design. However, by inspecting the plots of normal force and cam profile, shown in Figures A-5 and A-7, the worst case appears to occur at the end of the scan. At this point, the normal force is 12.7 pounds,

the cam curvature is approximately 0.5 inch, and $R_2 = 0.5$ inch and $R_2' = \infty$. For a 0.312 diameter follower with a spherical radius, $R_1 = R_1' = 0.156$ inch. Using these values of R_1 , R_2 and P_1 , and assuming steel is used for both materials, the coefficients given in Reference A-3 are listed below:

$K_D = 0.101211$	$\lambda = 0.746253$
$C_E = 6.067 (10^{-8})$	$C = 0.004690794$ inch
$\cos \theta = 0.134948$	$d = 0.003912263$ inch
$\alpha = 1.097958$	$Y = 0.00013458$ inch
$B = 0.915730$	$\max \sigma_c = 330,423$ psi

A significant reduction in the hertz stresses could be obtained by using a larger crown radius on the follower bearing. The 0.156 spherical radius was used in this analysis because, as the follower cocks at an angle to the cam surface, the center point of the follower always remains a constant 0.156 inch from the cam surface. If a larger crown radius is used, the follower cocks at an angle to the cam and rocks up on the larger radius. The distance from the center of the follower bearing to the cam surface changes with the angle. This procedure makes the mathematical relationships describing the cam profile, pressure angle, and other parameters very difficult to solve.

Further study in this area would pay large dividends in terms of reducing the stresses. As an example, for a 0.3125 outside diameter bearing with a width of 0.1094, the largest crown radius which can be put on the bearing will have a cord length of 0.1094 minus a clearance of approximately 0.020 on each edge to allow for tolerances and contact area, or about 0.0694 inch. The angle subtended by this cord is the total angular displacement of the elevation mirror which is 14.446386 degrees and corresponds to a radius of 0.276 as illustrated in Figure A-8.

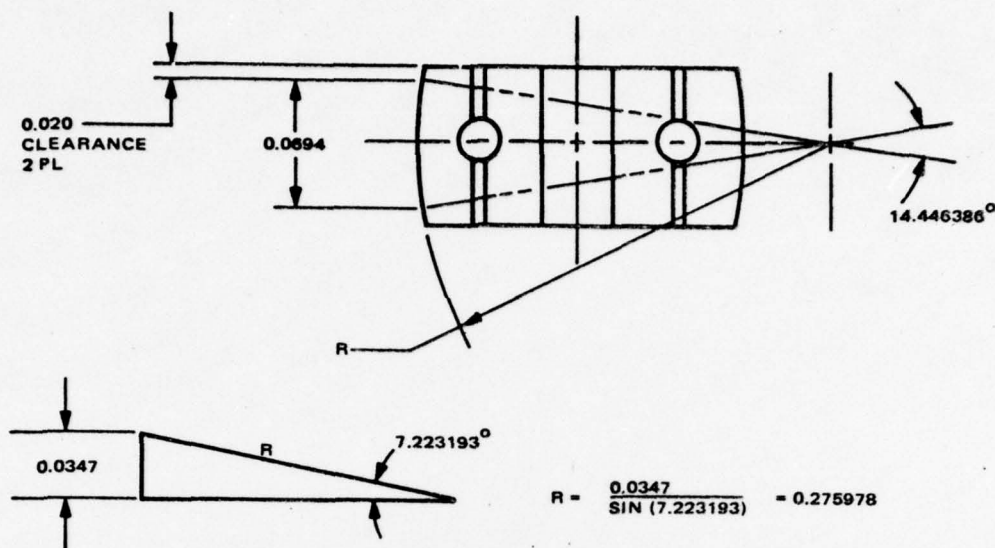


Figure A-8. Elevation mirror angle.

The results of $R_1 = 0.156$, $R_1' = 0.276$, $R_2 = 0.5$, $R_2' = \infty$ and $P = 12.7$ pounds (Reference A-3) are

$K_D = 0.124653$	$C_E = 6.067 (10^{-8})$
$\cos \theta = 0.397814$	$C = 0.006175995$ inch
$\alpha = 1.348617$	$d = 0.003526945$ inch
$B = 0.770159$	$y = 0.000121$ inch
$\lambda = 0.721284$	$\max \sigma_c = 278,381$ psi

This diagram represents a reduction in stress of 16 percent over the 330,423 psi.

FATIGUE LIFE

The allowable stresses may be estimated using the data presented by Morrison in Reference A-5. Although these data are only applicable to two cylindrical surfaces in contact, due to the lack of more applicable data, it should be used as a guideline only for a sphere in contact with a cylinder.

To use Morrison's data the percent of sliding between the two rolling surfaces must be known. For the cam design being analyzed, this percentage is equal to the amount the lever arm changes in Figure A-5, minus the amount the follower bearing rolls on its spherical radius. The result calculates as

0.190395 inch relative sliding per 360 degrees of cam rotation. The circumference of the cam was measured from Figure A-7 using a piece of string and is approximately 2.44 inches. The percent of sliding is $(0.190/2.44) \times 100 = 7.8$ percent. The values Morrison gives for 9 percent sliding will be used.

The Hertz stresses for two cylinders in contact is given by

$$S_C^2 = \frac{0.35 K}{\frac{1}{E_1} + \frac{1}{E_2}}$$

$$\text{and } \log_{10} K = \frac{B - \log_{10} N}{A}.$$

The highest endurance limit Morrison lists in his table is for 4140/4150 steel and 350 to 370 Bhn in contact with a tool steel roll hardened to 60 to 62 R_c . For these materials with 9 percent sliding, $A = 17.76$ and $B = 80.00$. N , for TWS, at 50 cycles per second for 2000 hours = $3.6 (10^8)$ cycles. Substituting these values for N , A , and B into the above formulas gives

$$K = 10537.33$$

and

$$S_C = 235,204 \text{ psi}$$

which is considerably under the existing 330,423 psi calculated in the last section.

Using a stress of 330,423 psi the above formulas predict that the life would be 2054 cycles or 41 seconds. Thus, the present design must be iterated to meet the design goal of 2000 hours mean time between failures.

FOLLOWER BEARING BASIC DYNAMIC LOAD RATING

In addition to the hertz stresses on the external surface of the follower bearing another design consideration is the required basic dynamic capacity, given in Reference A-6.

$$\text{required basic dynamic capacity} = \text{load on bearing} \times \text{speed factor} \times \text{life factor}$$

$$\times \text{race rotation factor} \times \text{hardness factor}$$

Since life is inversely proportional to $P^{10/3}$, Smith (Reference A-4) recommends using a root mean load given by

$$P = \sqrt[10]{\frac{L_1^{10/3} T_1 + L_2^{10/3} T_2 + \dots + L_n^{10/3} T_n}{100}}$$

where L = actual load and T = percent of total operating time.

The load, as shown in Figure A-5, was raised to the $10/3$ power and integrated using the trapezoidal rule and 200 trapezoids which gave a root mean load of

$$P = 8.245 \text{ pounds}$$

The speed of the follower bearing is faster than the cam because of its smaller circumference. The cam circumference can be measured from Figure A-7 as 2.44 inches and the cam speed is 3000 rpm. The speed of a 0.312 diameter follower would, therefore be

$$N = \frac{(3000)(2.44)}{(\pi)(0.312)} = 7468 \text{ rpm}$$

The speed factor is calculated from

$$SF = \left(\frac{N}{33^{1/3}} \right)^{0.3} = \left(\frac{7468}{33^{1/3}} \right)^{0.3} = 5.071$$

The life factor is calculated from

$$FL = \left(\frac{L}{500} \right)^{0.3} = \left(\frac{8.245}{500} \right)^{0.3} = 1.516$$

The race rotation factor for a rotating outer race is

$$RF = 1.1$$

The hardness factor for R_c 58 is

$$HF = 1.0$$

The required BDC is therefore,

$$BDC = (8.245) (5.071) (1.516) (1.1) (1.0) = 69.723 \text{ pounds.}$$

Also, since the loading curve of Figure A-5 has rapid variations in force it may be desirable to use a shock factor. Smith recommends a factor of 1.5 for light shock, giving a required BDC of

$$BDC = 1.5 \times 69.723 = 104 \text{ pounds.}$$

Further analysis is necessary to determine the need of the 1.5 shock loading factor. The 69 pound requirement could be met by a New Hampshire S154, which is a 0.3125 outside diameter full complement bearing with a BDC of 90 pounds. If the 104-pound BDC appears necessary, a larger bearing will have to be used and will cause a significant increase in the total rotational inertia of the elevation mirror.

CAM TORQUE

The necessary torque to drive the cam can be found using the principle of virtual work

$$\text{Torque} \times \text{Angle of Cam} = \text{Force} \times \text{distance of follower}$$

or

$$T d\phi = F dS$$

dividing by time, dt ,

$$T \frac{d\phi}{dt} = F \frac{dS}{dt}$$

or

$$T W = F V$$

$$\therefore T = \frac{F V}{W}$$

where:

T = torque about camshaft.

F = force on follower.

V = follower velocity from Figure 2, equation 2.

W = cam angular velocity = 314.159 rad/sec.

The torque versus cam angle is shown in Figure A-9.

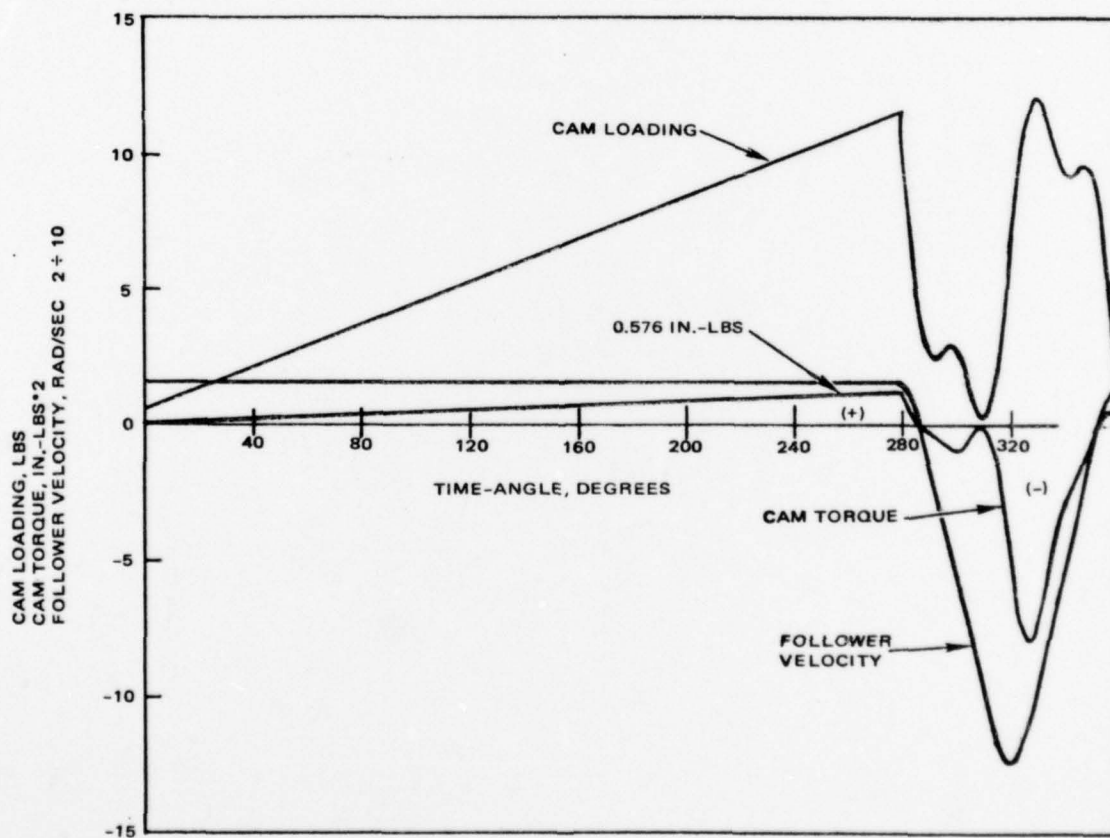


Figure A-9. TWS scanner.

The peak positive torque occurs at the end of the constant velocity scan portion of the cycle where the return spring is extended to almost its maximum value (a 0.239° overshoot at the end of the scan exists as the follower velocity changes direction) and the velocity is the constant scan velocity. The peak positive torque is

$$T = \frac{FV}{W} = \frac{(11.6 \text{ lb}) (15.708 \text{ in/sec})}{314.159 \text{ rad/sec}}$$

$$= 0.576 \text{ in-lbs.}$$

Note that during spin-up, V and W will not have reached the values shown in the equation, but the ratio will still be 15.708/314.159.

After the displacement reaches its maximum value, i. e. , "gets over the hump", the torque becomes negative, as shown in Figure A-9. This change indicates that the follower drives the cam causing the azimuth wheel speed to increase.

The cam torque is primarily of interest during spin-up where the motor must supply the torque to "get over the hump". Once the cam shaft has reached some velocity, this energy could come from the kinetic energy of the cam shaft requiring a smaller motor size. At the time of turn-on the follower will always be on the lowest point of the cam. Being pushed downhill by the return spring, the motor will have a running start at the peak, and therefore, will only need to produce a torque equal to the average torque of Figure A-9 which is 0.299 in-lbs. The final motor size is still being evaluated using these considerations in conjunction with friction, windage, and spin-up time requirements.

SPEED FLUCTUATION

An estimate of the speed change due to the alternate absorption and emission of energy by the return spring was made and is shown plotted versus time in Figure A-10. The math model assumes that the motor only puts out enough torque to overcome friction and windage, and that all of the energy to compress the return spring comes from the kinetic energy of the azimuth shaft. This action causes the azimuth shaft to alternately slow down then

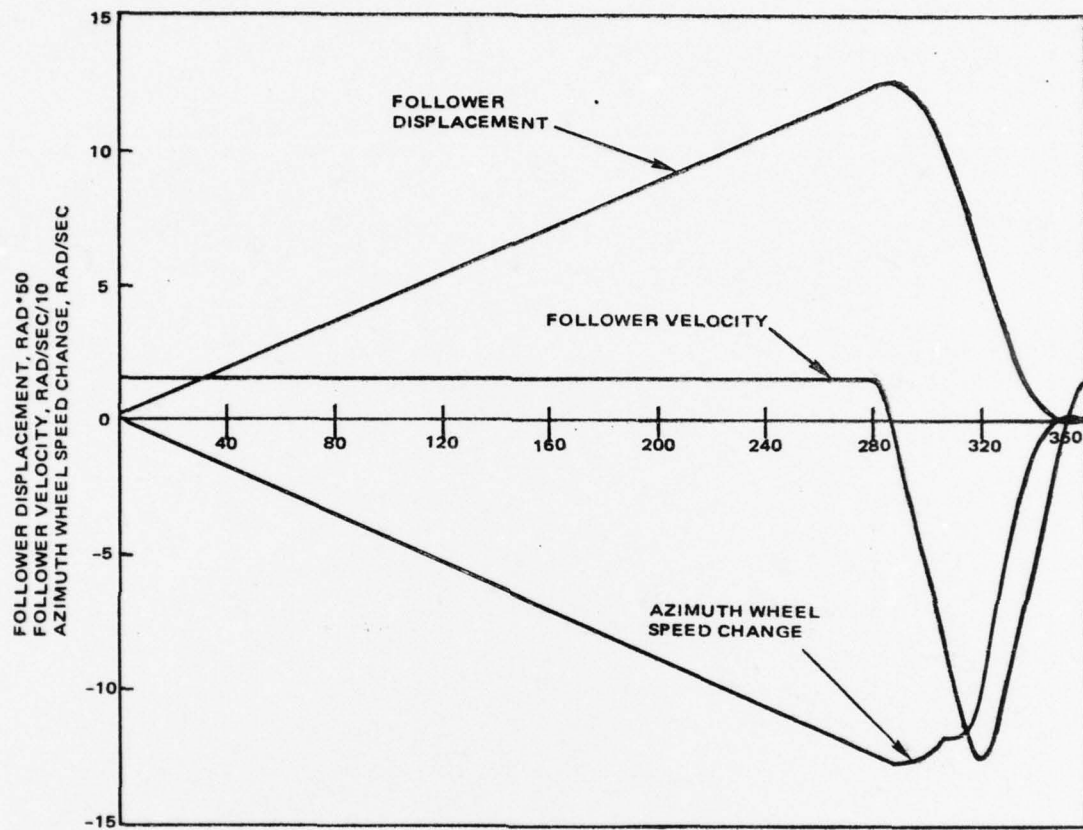


Figure A-10. TWS scanner.

speed up as the return spring compresses and expands. The model also neglects the speed fluctuation of the elevation mirror because its kinetic energy is small compared to the azimuth shaft. Its speed will change by the same ratio that the azimuth speed changes, or about 4 percent maximum.

The math model for the speed change is

$$KE + PE = \text{constant} = 19.197 \text{ in-lbs.}$$

$$KE = \frac{I_{AZ} W_{AZ}^2}{2} + \frac{I_{EL} W_{EL}^2}{2}$$

$$PE = 22.35 \theta^2 + 0.450 \theta$$

Substituting and solving for W_{AZ} gives,

$$W_{AZ} = \sqrt{\frac{2}{I_{AZ}} \left(19.197 - 22.35 \theta^2 - 0.45 \theta - \frac{I_{EL} W_{EL}^2}{2} \right)}$$

where:

KE = kinetic energy.

PE = potential energy of spring.

I_{AZ} = inertia of camshaft, motor, and azimuth facet wheel.
= $3.887 (10^{-4}) \text{ in-lb-sec}^2$.

I_{EL} = inertia of elevation mirror = $1.113 (10^{-4}) \text{ in-lb-sec}^2$.

W_{AZ} = angular velocity of camshaft,

W_{EL} = angular velocity of elevation mirror from Figure A-2,
equation 2.

θ = angular displacement of elevation mirror from
Figure A-2, equation 1.

REFERENCES

- A-1. Jason H. Fan, "NAVFLIR Cam Design," IDC 2704/389, November 17, 1970.
- A-2. Francis H. Raven, "Analytical Design of Disk Cams and Three-Dimensional Cams by Independent Position Equations," ASME Transactions, Vol. 26, Series E, No. 1, March 1959, pp. 18-24.
- A-3. Raymond J. Roark, Warren C. Young, "Formulas for Stress and Strain," Fifth Edition, pg. 518, Case 4.
- A-4. Richard J. Smith, "Cam Followers - Think of Them as Heavy Duty Bearings," Machine Design, October 3, 1974, pp. 106-109.
- A-5. Ralph A. Morrison, "Load/Life Curves for Gear and Cam Materials," Machine Design, August 1, 1968, pp. 102-108.
- A-6. Torrington Bearing Catalog.

$$19.197 - 22.35 \theta - 0.45 \theta - \frac{\theta^2}{2})$$

gy.

energy of spring.

camshaft, motor, and azimuth facet wheel.

10^{-4}) in-lb-sec².

elevation mirror = $1.113 (10^{-4})$ in-lb-sec².

locity of camshaft,

locity of elevation mirror from Figure A-2,

placement of elevation mirror from
2, equation 1.